ORNL/TM-2017/740

Mechanical Properties and Radiation Resistance of Nanoprecipitates-Strengthened Advanced Ferritic Alloys

Lizhen Tan
Ying Yang
Tianyi Chen
Oak Ridge National Laboratoy

Kumar Sridharan
Li He
University of Wisconsin-Madison

December 30, 2017

OAK RIDGE NATIONAL LABORATORY
MANAGED BY UT-BATTELLE FOR THE US DEPARTMENT OF ENERGY

ORNL/TM-2017/740
M2CA-15-TN-OR0402023

Nuclear Energy Enabling Technologies (NEET): Reactor Materials
FY 2015 Award

MECHANICAL PROPERTIES AND RADIATION RESISTANCE OF NANOPRECIPITATES-STRENGTHENED ADVANCED FERRITIC ALLOYS

Lizhen Tan, Ying Yang, Tianyi Chen
Oak Ridge National Laboratory

Kumar Sridharan, Li He
University of Wisconsin-Madison

Date Published: December 30, 2017

Prepared by
OAK RIDGE NATIONAL LABORATORY
Oak Ridge, TN 37831-6283
managed by
UT-BATTELLE, LLC
for the
US DEPARTMENT OF ENERGY
under contract DE-AC05-00OR2272

CONTENTS

Page

LIST OF FIGURES

LIST OF TABLES

Acknowledgments

This research was sponsored by the U.S. Department of Energy (DOE), Office of Nuclear Energy (NE), the Nuclear Energy Enabling Technologies (NEET) program, Reactor Materials FY 2015 Award. We gratefully acknowledge the support provided by Sue Lesica of DOE-NE and Stuart Maloy of Los Alamos National Laboratory.

The authors are grateful to Tom Geer and Douglas Stringfield of Oak Ridge National Laboratory (ORNL) for sample preparation, and Samantha Joers of the University of Wisconsin-Madison for assistance in ion-irradiation sample preparation and some characterization. Philip Maziasz and Xiang Chen of ORNL are appreciated for technical review of this report.

EXECUTIVE SUMMARY

Five ferritic alloys and a ferritic-martensitic steel, designed by computational thermodynamics using recently developed database, were assessed in this work. A previous Fe-Cr-Zr ferritic alloy, named as Z6, was further investigated because of its amorphization behavior after a peak damage of 50 displacements per atom (dpa) at 400°C. Alloying elements of Zr, Nb, and Mo were varied to form four new ferritic alloys, named as Z1N33A, BL-Nb, BL-NbZr, and BL-Mo, which have reduced Zr-bearing Laves phase and complemented with B2-NiAl phase. The ferritic-martensitic steel, named as TTZ2M, favored MX-type (M=metal, X=C/N) precipitates with controlled $M_{23}C_6$ and Laves phases.

Tensile tests were conducted in air from ambient up to 800°C. Creep tests were performed in air at 650°C, primarily with 120 and 100 MPa loads. The tests indicated noticeable enhancement for TTZ2M and BL-Nb compared to the other alloys and reference steel T91. Nanoindentation measurements on alloy Z6 revealed differences in mechanical properties of the intermetallic and matrix ferritic phases.

Microstructural characterization showed Laves and B2 phases with varied sizes and densities in the ferritic alloys. It was found that a high density of Laves phase, primarily in micrometer sizes decorating grain boundaries, was detrimental to the ductility of ferritic alloys. However, fine Laves phase, smaller than a couple of hundred nanometers, could benefit creep resistance. Ultrafine B2 phase (e.g., ~10 nm) alone, e.g., in BL-Mo, was not likely to be an effective component to enhance creep resistance. A combination of ultrafine with coarse precipitates tended to yield superior creep resistance, e.g., BL-Nb.

Post-irradiation examinations showed that the B2 phase in the BL-series alloys were stable after irradiation up to 220 dpa at 475°C, whereas the Laves phase underwent amorphization and disintegration. Radiation-induced amorphization in the intermetallic phases (i.e., Laves and $Fe_{23}Zr_6$) resulted in changes in deformation mechanisms as manifested by nanoindentation on Z6. Radiation-induced hardening took place in all the examined alloys, with the least hardening in TTZ2M, followed by BL-Nb, and the greatest hardening in Z1N33A. This is in agreement with the increased density of dislocations in the irradiated samples as revealed by TEM characterizations. Voids were not observed in the examined alloys, suggesting superior swelling resistance of the alloys compared to T91 irradiated at a similar condition.

To better understand the microstructure-property relationship, near-term future work will include:

- Characterize the creep-ruptured samples to reveal the effect of particle size (e.g., ~10–50 nm B2; ~250 nm and larger Laves) on their interactions with dislocations and failure;
- Understand the role of Zr and Mo on the formation of the precipitates;
- Optimize and fabricate two larger heats (one TTZ2M and one from the BL-series) for better microstructure control with thermomechanical treatments and detailed assessment.

1. INTRODUCTION

Advanced nuclear reactors as well as the life extension of light water reactors require advanced alloys capable of satisfactory operations up to neutron damage levels approaching 200 displacements per atom (dpa) [1]. Extensive studies, including fundamental theories, have demonstrated the superior resistance to radiation-induced swelling in ferritic steels, primarily inherited from their body-centered cubic (bcc) structure [2]. In our previous work [3], novel Fe-Cr-Zr ferritic alloys strengthened by Fe_2Zr_based Laves phase precipitates showed superior strength, ductility, and creep resistance at high temperatures, however, a consistent improvement on their radiation resistance data has yet to be achieved. Preliminary self-ion irradiation at 400°C exhibited amorphization of some phases in the Fe-Cr-Zr ferritic alloys.

The previously developed Fe-Cr-Zr-based alloys exhibited a considerable amount of Fe_2Zr-type Laves phase and decent property improvement. However, those Fe_2Zr-type Laves phase were generally in micrometers. To further improve properties, ferritic alloys with refined precipitates were explored in this study, by reducing Zr content to lower the precipitation temperature of the relevant precipitates. To compensate the strength reduction induced by the Zr content reduction, a new type of precipitates, B2 phase, was introduced to be coherent with the bcc matrix.

This report summarizes the mechanical properties, radiation resistance and relevant microstructural characterization of the designed alloys.

2. EXAMINED ALLOYS AND EXPERIMENTAL METHODS

2.1. Examined alloys

Based on the results of the previously studied alloys, several ferritic and ferritic-martensitic steels were designed using the recently developed thermodynamic database [4]. The nominal compositions in weight percentage (wt.%) of the alloys are listed in Table 1.

Table 1. Designed alloys to be screened.

Alloy ID	Nominal composition (with Fe balance)	Alloy type
Z6	9Cr-1W-11Zr	Ferritic
Z1N33A	12Cr-3W-3Ni-3Al-1Zr	Ferritic
BL-NbZr	12Cr-3W-3Ni-3Al-1Nb-0.15Zr	Ferritic
BL-Nb	12Cr-3W-3Ni-3Al-1Nb	Ferritic
BL-Mo	12Cr-3W-3Ni-3Al-1Mo	Ferritic
TTZ2M	8.5Cr-1.3W-0.1V-0.15Ti-0.05Ta-0.1C	Ferritic-martensitic

The calculated temperature-dependent phase fractions of the alloys are plotted in Figure 1. Figure 1a shows alloy Z6, being composed of a large amount of Laves phase in ferrite (α) matrix. In contrast, the additions of Ni and Al lead to the formation of B2-phase, e.g., NiAl, in Z1N33A (Fig. 1b), BL-NbZr (Fig. 1c), BL-Nb (Fig. 1d), and BL-Mo (Fig. 1e). The addition of W and reduction of Zr in the alloys resulted in reduced Laves phase. It's interesting to note that a small amount of Zr addition in alloy BL-NbZr (Fig. 1c) would introduce a small amount of Ni_7Zr_2 phase, which is not expected in the alloys with higher Zr content. Unlike the ferritic alloys, ferritic-martensitic steel TTZ2M (Fig. 1f) has a decent temperature range of austenite (γ), in which MX (M=metal, X=C/N) phase dissolves during high-temperature normalization and starts to precipitate during cooling and follow-up tempering treatment.

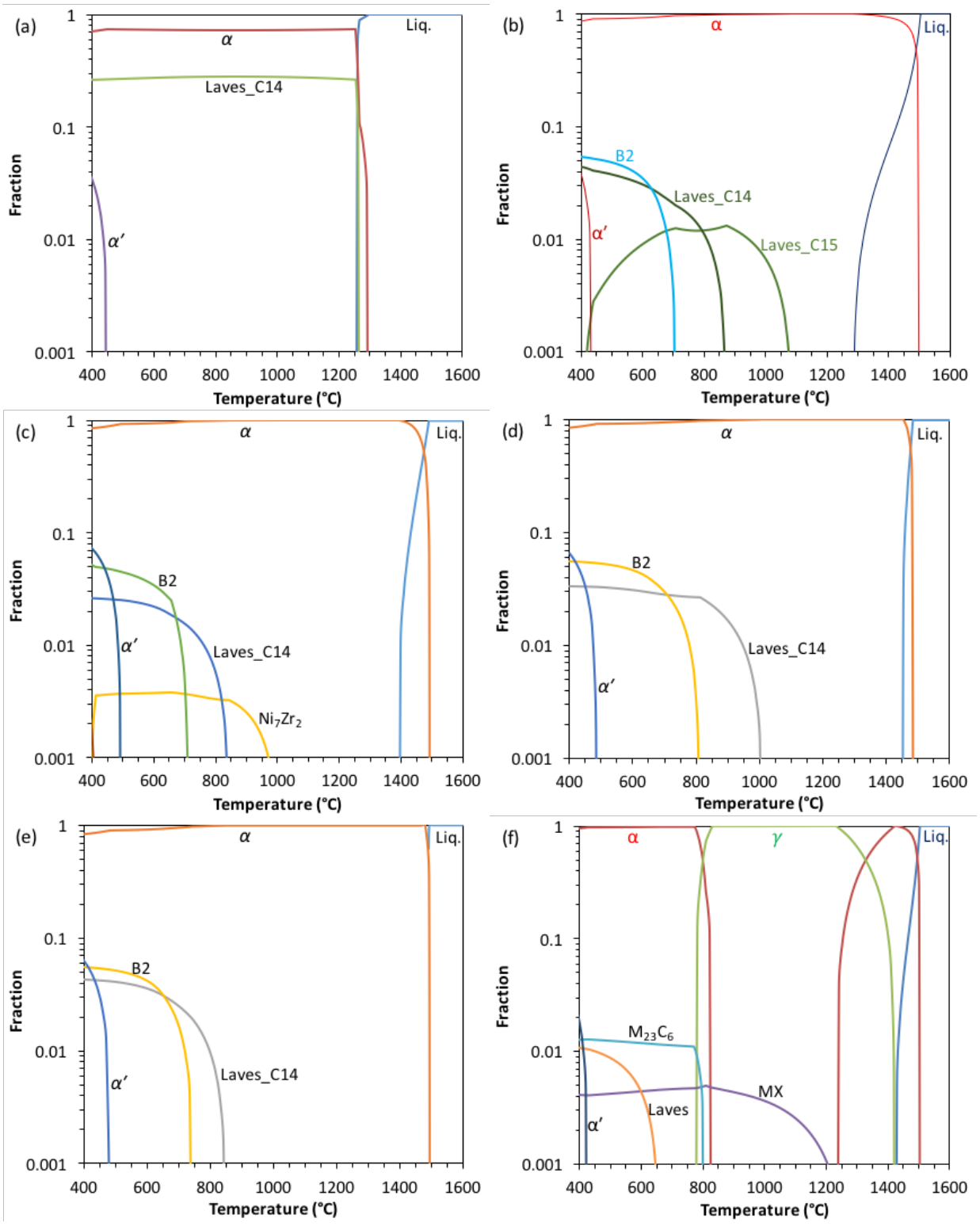

Figure 1. Calculated temperature-dependent phase fractions in alloys (a) Z6: Fe-9Cr-1W-11Zr, (b) Z1N33A: Fe-12Cr-3W-3Ni-3Al-1Zr, (c) BL-NbZr: Fe-12Cr-3W-3Ni-3Al-1Nb-0.15Zr, (d) BL-Nb: Fe-12Cr-3W-3Ni-3Al-1Nb, (e) BL-Mo: Fe-12Cr-3W-3Ni-3Al-1Mo, and (f) TTZ2M: Fe-8.5Cr-1.3W-0.1V-0.15Ti-0.05Nb-0.1C.

2.2. Experimental methods

Mechanical tests of the alloys include tensile, creep, and nanoindentation. Type SS-3 miniature specimens with a gauge section of 7.62 × 1.52 × 0.76 mm were extracted from the alloys for tensile and creep tests, with the specimen length aligned with the longitudinal direction of the alloy heats.

- Tensile tests were conducted in air using shoulder load at a crosshead-controlled strain rate of 0.001 s^{-1} from room temperature up to 800°C in accordance with the American Society of Testing and Materials (ASTM) standard E8/E8M-13a (*Standard Test Methods for Tension Testing of Metallic Materials*) and E21/E21M-09 (*Standard Test Methods for Elevated Temperature Tension Tests of Metallic Materials*).
- Creep tests were conducted in air using shoulder load at 650°C with different loads.
- Nanoindentation was previously conducted on Alloy Z6 at room temperature to probe the mechanical properties of the intermetallic phases. In this report, we included detailed microstructure analysis within the deformed region, addressing the effect of irradiation on deformation mechanisms.
- Fe^{2+} ion irradiation was conducted to Z1N33A and the BL series of samples at the ion beam lab, Universit of Wisconsin-Madison. The irradiation temperature was 475 °C and the nominal peak damage was 220 dpa with the ion energy being 4 MeV. Post-irradiation examinzations were conducted through microstructural characterization and nanoindentation measurements.

Scanning electron microscopy (SEM), transmission electron microscopy (TEM), and energy dispersive x-ray spectroscopy (EDS) were employed to investigate the as-received, deformed and irradiated samples. As will be detailed later, such investigation provides insights into the roles of precipitates on strengthening the materials. Focus-ion beam (FIB) technique was used to prepare electron transparent lamellae for TEM characterization.

3. MECHANICAL PROPERTIES

3.1. Tensile properties

Figure 2 plots the temperature-dependent yield strength, tensile strength, uniform plastic elongation, and total plastic elongation of the 6 alloys. Literature data of P91 are included as a reference [5]. Compared to the same category alloy P91, alloy TTZ2M exhibited noticeably greater strength without much compromise in ductility. The ferritic alloys showed more or less increases in strength, especially tensile strength, compared to TTZ2M, but generally lower ductility at temperatures <400°C. The inset of Fig. 2a-b shows the gauge cross-section of the SS-3 specimens tested in this work and the round dogbone-shaped specimens tested for P91. The small SS-3 with four sharp-right-angle corners would somewhat impair the ductility compared to the round specimens. Comparing the alloys tested using SS-3, however, the lower ductility of the ferritic alloys at low temperatures is likely attributable to the too many coarse particles decorating the grain boundaries, which is presented in the next section. The amount of such coarse particles is to be reduced in new alloys.

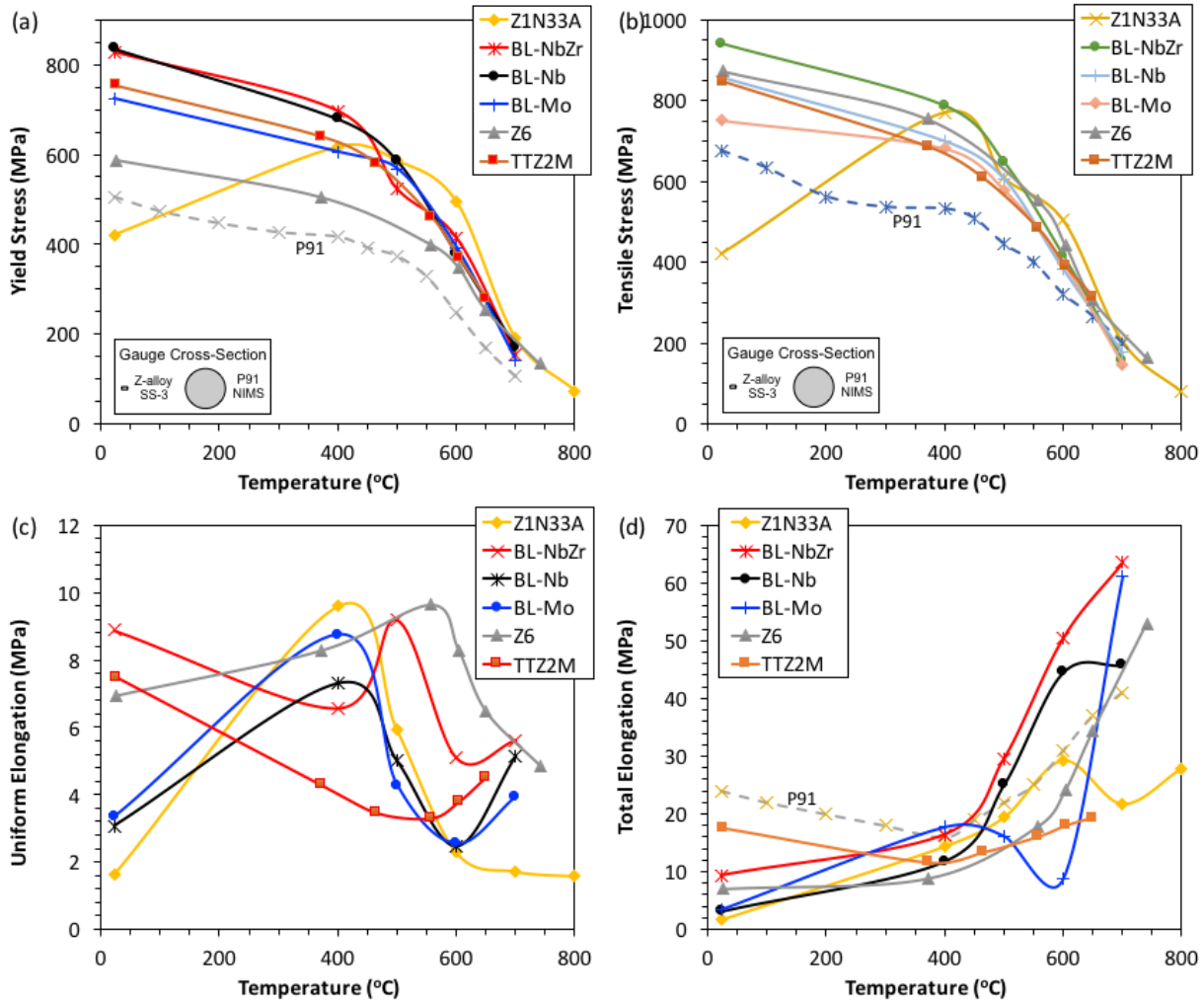

Figure 2. Temperature-dependent (a) yield strength, (b) tensile strength, (c) uniform elongation and (d) total elongation of the ferritic and ferritic-martensitic alloys, compared to literature data of P91.

3.2. Creep resistance

Figure 3 shows the creep curves of the designed alloys tested at 650°C with loads of 120 and 100 MPa. Samples of T91, extracted from a commercial T91 heat of Nippon Steel & Sumitomo Metal Corporation, were also tested using the same creep frame for comparison. Alloy Z6 (not shown here) was only tested at 110 MPa and 650°C, yielded 665 h creep rupture life, which suggests its superior creep resistance than all the other designed alloys. However, the development of the solely Fe_2Zr-strengthened alloy was discontinued because of its intrinsically low ductility at low temperatures. The 650°C and 100 MPa tests of Z1N33A, BL-NbZr, and BL-Mo were not started yet. Figure 3 indicates that the BL-Nb (with an ongoing test at 650°C and 100 MPa) and TTZ2M have noticeably superior creep resistance than T91. The other ferritic alloys Z1N33A, BL-NbZr, and BL-Mo had better or worse creep resistance compared to T91, which is likely attributable to the too many coarse particles decorating the grain boundaries as presented in the next section.

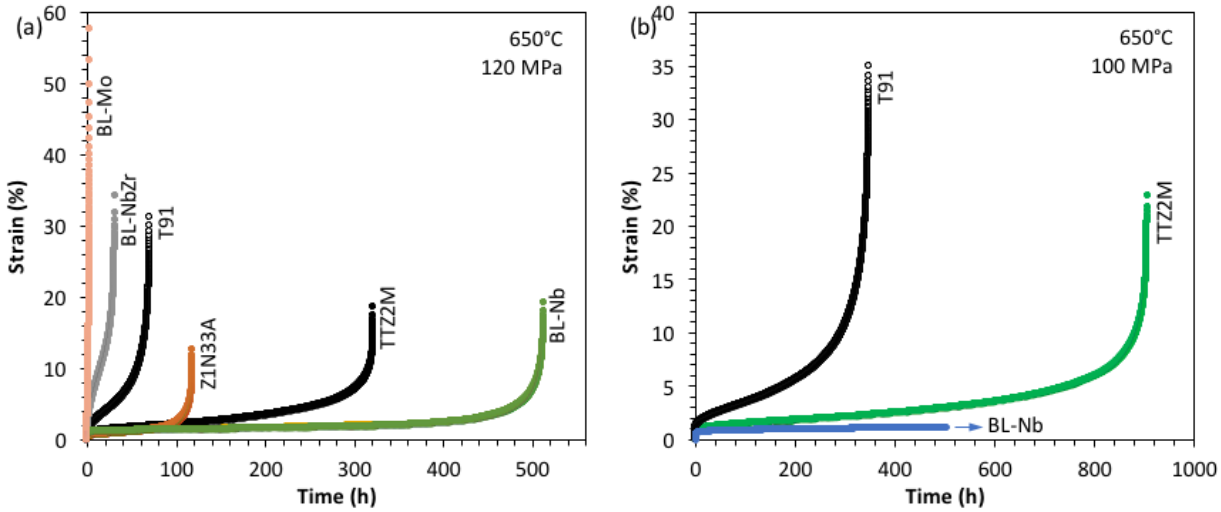

Figure 3. Creep curves of the examined alloys tested in air at 650°C with loads of (a) 120 MPa and (b) 100 MPa.

The minimum creep rates at the steady-sate creep stage of the samples were deduced and summarized in Table 2. The superior creep resistance of TTZ2M and BL-Nb is clearly manifested by their low minimum creep rates at the test conditions.

Table 2. Minimum creep rates (h^{-1}) of the designed alloys compared to T91 tested at 650°C.

Alloy ID	120 MPa	100 MPa
Z1N33A	1.06×10^{-4}	
BL-Mo	5.39×10^{-2}	
BL-NbZr	4.29×10^{-3}	
BL-Nb	1.93×10^{-5}	5.68×10^{-6}
TTZ2M	8.72×10^{-5}	2.97×10^{-5}
T91	1.04×10^{-3}	1.72×10^{-4}

3.3. Nanoindentation results

Nanoindentation was conducted on alloy Z6 sample to investigate the deformation responses of different phases. Prior to indentation, the sample was mechanically polished to have a mirror-condition surface with 0.02 μm colloidal silicon being used for the final step. In total, 109 indents were conducted on the sample. Figure 4a shows the representative displacement curves for the three phases, namely, ferritic (Fe-Cr body-centered cubic), Laves present (Fe_2Zr) and $Fe_{23}Z_6$, in alloy Z6. The two intermetallic phases have higher hardness, as the load is higher at the same indentation depth for the intermetallic phases than the ferrite. The hardness distribution is plotted in Figure 4b to further show the difference in mechanical properties of the three phases.

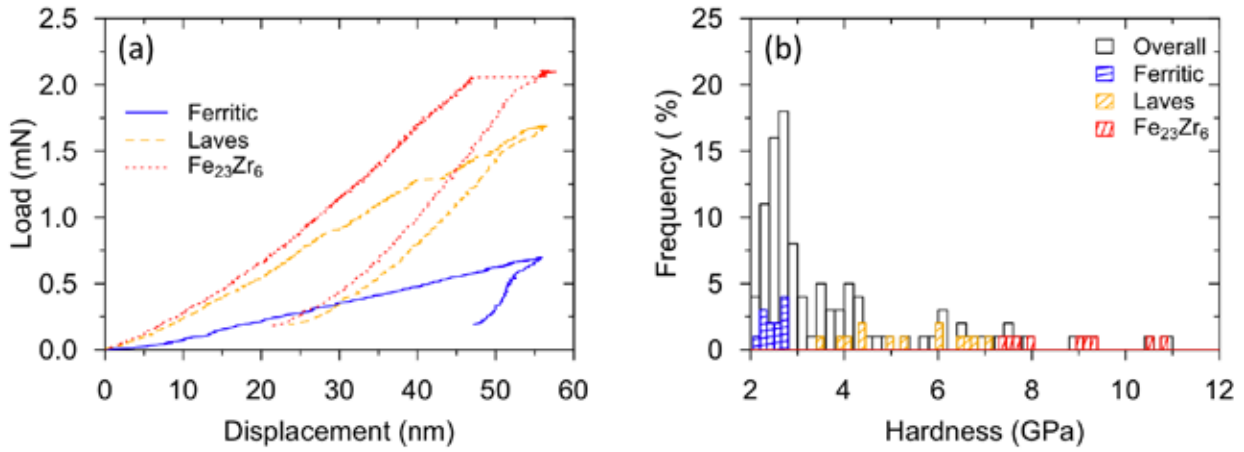

Figure 4. Nanoindentation (a) load-displacement curves and (b) hardness distributions of the ferrite, Laves, and $Fe_{23}Zr_6$ phases in alloy Z6.

Figure 4a also shows pop-in behavior for the intermetallic phases. The $Fe_{23}Zr_6$ phase shows a pop-in of ~10 nm at the load of ~2 mN. Such a phenomenon was generally observed in this phase. It is worth noting that very fine pop-ins of a couple of nm were also observed at lower load. Meanwhile, the Laves phase exhibited several pop-ins up to ~5 nm in the pop-in depth. The pop-ins are believed to be associated with defect formation, which will be revealed by electron microscopy and detailed in the next section.

4. MICROSTRUCTURAL CHARACTERIZATION

4.1. Alloy Z6

Figure 5a shows a high-angle annular dark-field micrograph of an alloy Z6 specimen. The Zr-containing intermetallic phases are shown with bright contrast because of their higher Z numbers. The solid and dashed arrows mark the $Fe_{23}Zr_6$ and Fe_2Zr phases, respectively. The two intermetallics have different morphology: the $Fe_{23}Zr_6$ phase, which takes a Th_6Mn_{23} crystal structure as illustrated by its electron diffraction pattern in Figure 5b, has coarse domains; whereas the Fe_2Zr phase, which takes a Laves-C14 crystal structure as illustrated by its electron diffraction pattern in Figure 5c, has finer domains decorated with strip features.

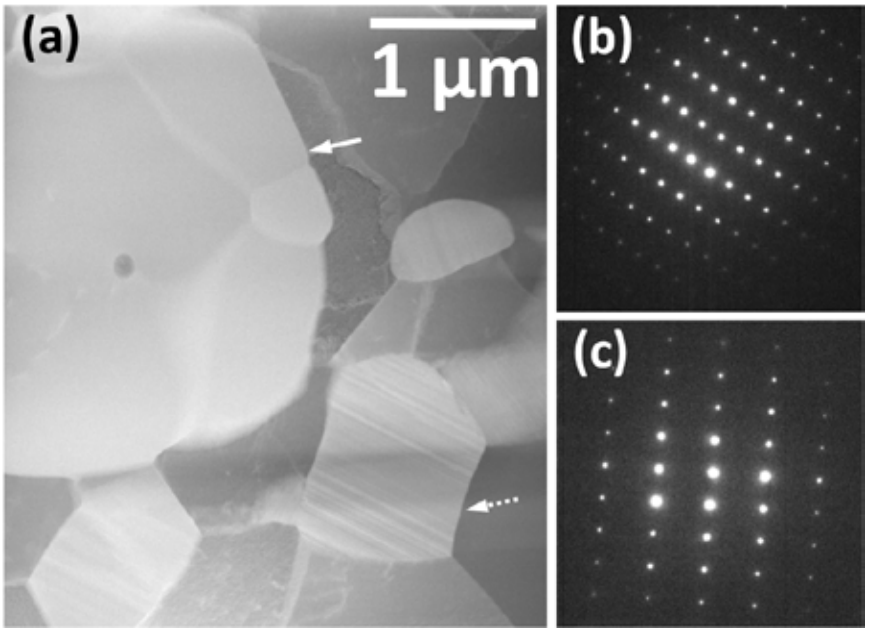

Figure 5. (a) HAADF micrograph of alloy Z6 showing different intermetallic phases with SAD patterns for the (b) $Fe_{23}Z_6$ on [013] zone and (c) C14 Laves phase on [-1100].

Figure 6 revealed the fine structure of the strip features in the Fe_2Zr phase. Figure 6a is a bright-field image taking at a two-beam condition putting the strips in contract. Selected area diffraction (SAD) patterns in Figure 6b and c were obtained from B and C areas in Figure 6a, representing the scenarios without and with strips, respectively. Figure 6b is the electron diffraction pattern at the [10-10] zone of the C14 Laves phase. Comparing with Figure 6b, the diffraction pattern in Figure 6c shows extra spot along the <0001> direction, indicating a different stacking of the basal plane, which converts the local crystal structure to be a C36 crystal structure. The C14 and C36 stacking was confirmed with high resolution scanning transmission electron microscopy (HR-STEM) presented in Figure 6d and e. The boxed regions in Figure 6d and e were zoomed in and compared to the projections of the C14 and C36 crystal structures, respectively, as shown in Figure 6f and g.

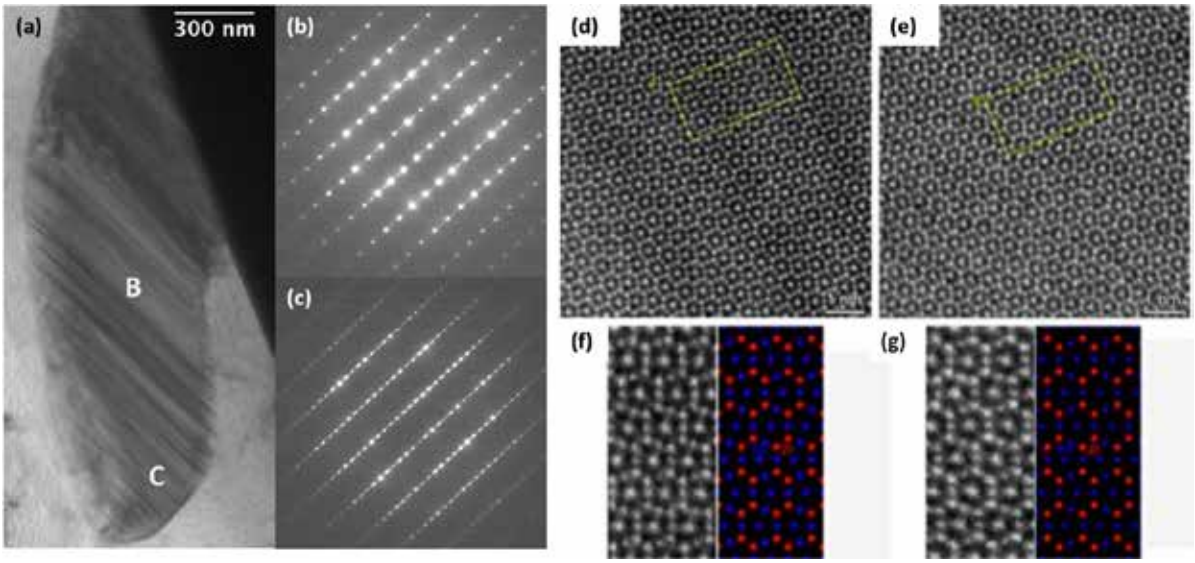

Figure 6. (a) Conventional bright-field image of alloy Z6 showing the Laves phase with a high density of stacking faults. (b-c) SAD patterns of the fault-free region (C14 structure) and faulted region (C36 structure), respectively. (d-e) HR-STEM images showing the C14 and C36 stacking, respectively. (f-g) Zoomed micrographs of the boxed regions in (d-e) with simulated structures illustrating the different stacking of C14 and C36, respectively.

Figure 7a shows the ex-situ STEM of indented $Fe_{23}Zr_6$ phase. The black triangle a top of the image schematically indicates the indentation location. It can be seen that high density of dislocations formed under the indentation. The prominent dislocation features were zoomed in and shown in Figure 7b and c, corresponding to the regions enclosed in the solid and dashed boxes in Figure 7a, respectively. With consideration of the crystal orientation, it can be seen in Figure 7b that dislocations seemed to inhabit on the {110} and {100} planes. On the other hand, 1/6<121>{111} faults were observed to form in a deeper region, approximately 350 nm from the indented surface. The formations of such dislocations are believed to be associated with the pop-in phenomena observed during indentation.

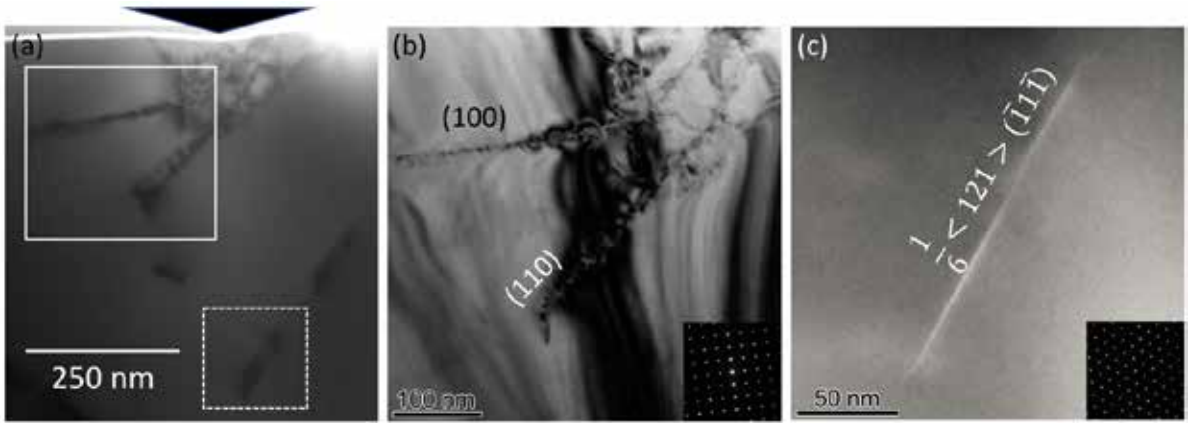

Figure 7. (a) STEM-BF image of alloy Z6 showing dislocation formation in response to nanoindentation of 60 nm depth. (b) conventional BF image showing the dislocations formed on (100) and (110) planes, in the solid boxed region of (a). (c) STEM-BF image showing 1/6<121> type stacking fault formation in the dashed boxed region of (a).

Figure 8 shows the ex-situ TEM of indented sample, focusing on the Fe_2Zr phase. Upon indentation, strip features of the indented region disappeared, indicating the stacking faults of C36 were removed through slip of the basal plane. The glide of a synchro-Shockley partial dislocation was believed to cause the change of the layer-stacking sequence, leading to local transformation from C36 to C14 structure, and accommodating the deformation induced by indentation along the basal plane [6]. Perpendicular to the basal plane, dislocations were observed to form inhabiting on the (11-20) plane, as seen in Figure 8b, imaged at a beam condition where the faults on the basal planes were not in contrast. A HRTEM of the dislocations on the (11-20) plane is presented in Figure 8c.

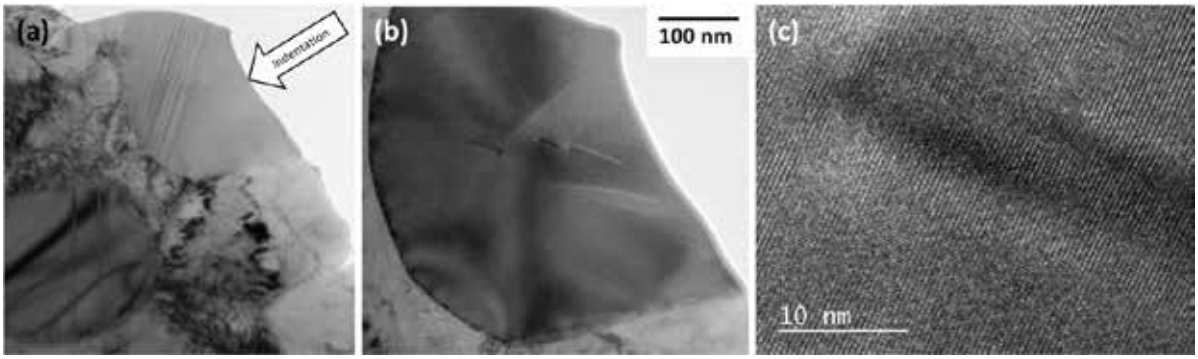

Figure 8. (a) BF image of alloy Z6 showing the microstructure evolution of the Laves phase in response to nanoindentation. (b) Dislocation formation in the deformed Laves domain. (c) HR image showing the dislocations in (b).

Amorphization of the intermetallic phases induced by self-ion irradiation to a peak damage of 50 dpa at 400°C has been observed in the past [7]. More details are revealed in the current study. Figure 9a shows HAADF images of an irradiated alloy Z6 specimen, with B and C marking the $Fe_{23}Zr_6$ and Fe_2Zr phases, respectively. After irradiation, the $Fe_{23}Zr_6$ phase became totally amorphous, as indicated by its ring pattern of SAD presented in Figure 9b. On the other hand, the Fe_2Zr phase was partially amorphous, showing a dim ring pattern superimposed on the diffraction spots of [-1100] zone.

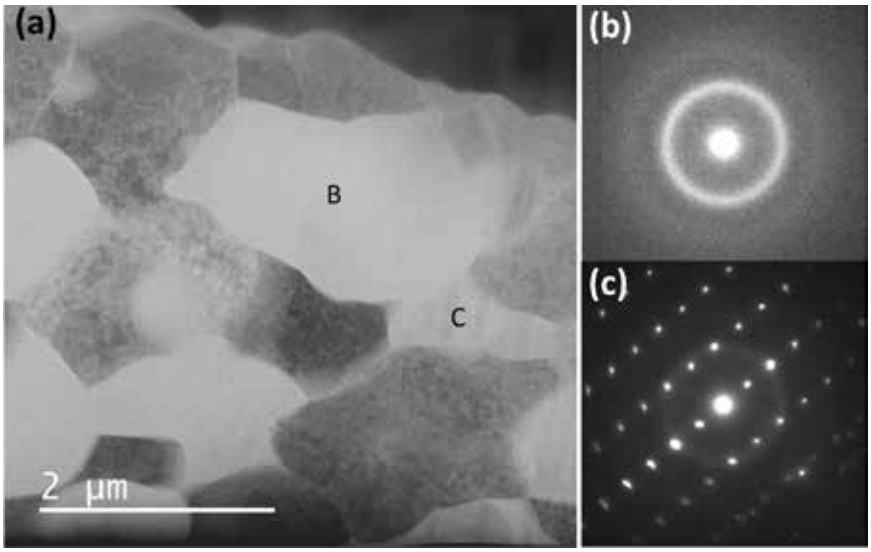

Figure 9. (a) HAADF image showing the microstructure of alloy Z6 after 50 peak dpa Fe^{2+} irradiation with SAD patterns indicating radiation-induced (b) total amorphization of $Fe_{23}Zr_6$ in domain B and (c) partial amorphization of Laves phase in domain C in (a).

Figure 10 shows in detail the partially amorphous structure of the Fe_2Zr phase. Figure 10a shows a Fe_2Zr domain that has a darker contrast. Within the domain, the bright features have crystalline structure as indicated by the converged beam electron diffraction (CBED) pattern shown in Figure 10c, whereas the rest part of the domain having a dark contrast are amorphous, as indicated by the ring pattern in CBED shown in Figure 10d. A HRTEM of the remaining crystalline is presented in Figure 10b, where high density of radiation-induced defects can be observed.

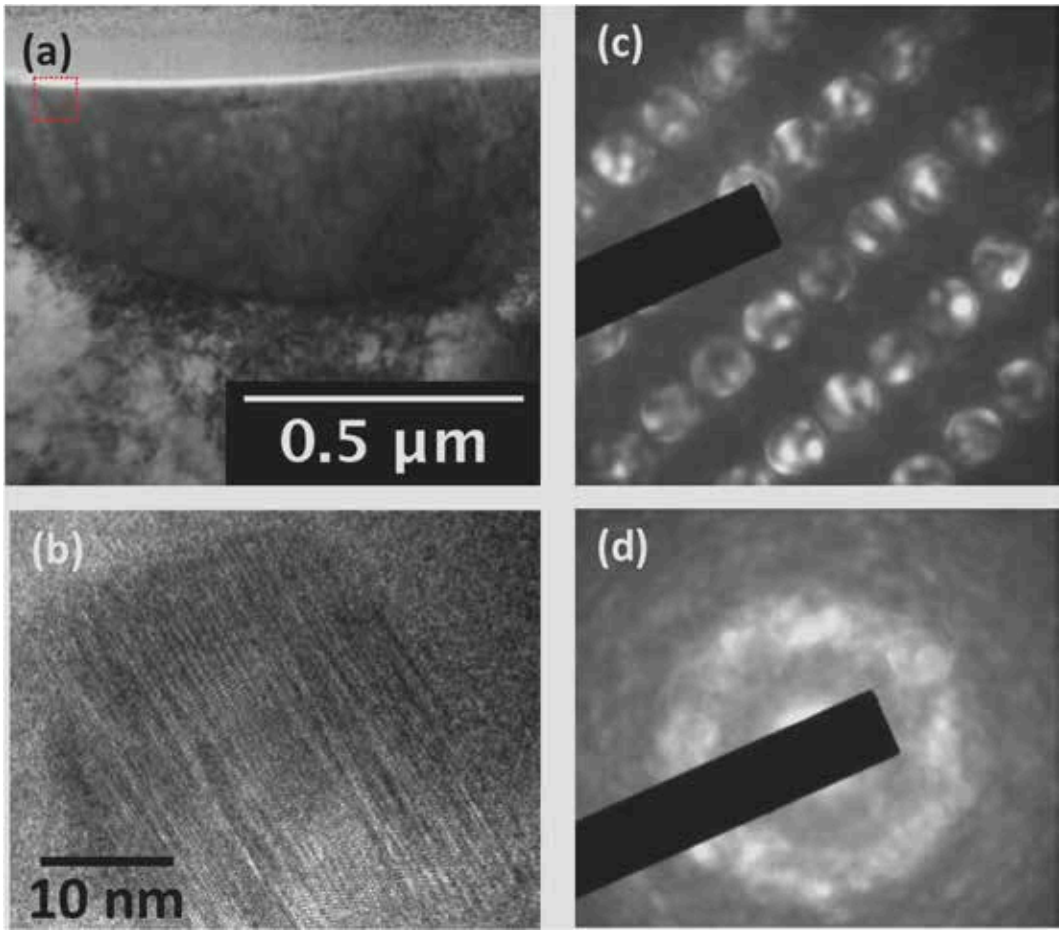

Figure 10. (a) Radiation-induced partial amorphization of the Laves phase in alloy Z6 with crystalline islands embedded in the amorphous domain. (b) HRTEM showing the crystalline of the dashed boxed region in (a). CBED patterns of (c) the crystalline showing the Laves structure and (d) the amorphous region.

The microstructure analysis of indented and irradiated Z6 sample revealed the deformation and radiation responses of the intermetallic phases of $Fe_{23}Zr_6$ and Fe_2Zr. Both intermetallic phases form dislocations under stress, which are firstly evidenced by the load-displacement curves and later confirmed by TEM investigation. In deformed $Fe_{23}Zr_6$ precipitates, 1/6<121>{111} type dislocation was observed, which suggests the activation of twinning deformation. In deformed Fe_2Zr precipitates, the pre-existing C36 faults disappeared after indentation, indicating the glide of synchro-Shockley partial dislocations plays a role in the deformation. Both intermetallic phases undergo amorphization during Fe-ion irradiation; the $Fe_{23}Zr_6$ phase became totally amorphous whereas the Fe_2Zr phase became partially amorphous.

4.2. Alloy Z1N33A

Figure 11 shows the microstructure of the Z1N33A after hot rolling at 1100°C followed by aging at 800°C and 650°C for 5 h. The distribution of the intermetallic precipitates, shown in bright in Figure 11, was observed primarily decorating grain boundaries along the rolling direction. Some local recrystallization was observed in Figure 11b, as fine grains of diameters on the order of 10 μm. The presence of the pronounced amount of intermetallic precipitates is believed to have impeded the recrystallization during thermal mechanical treatment.

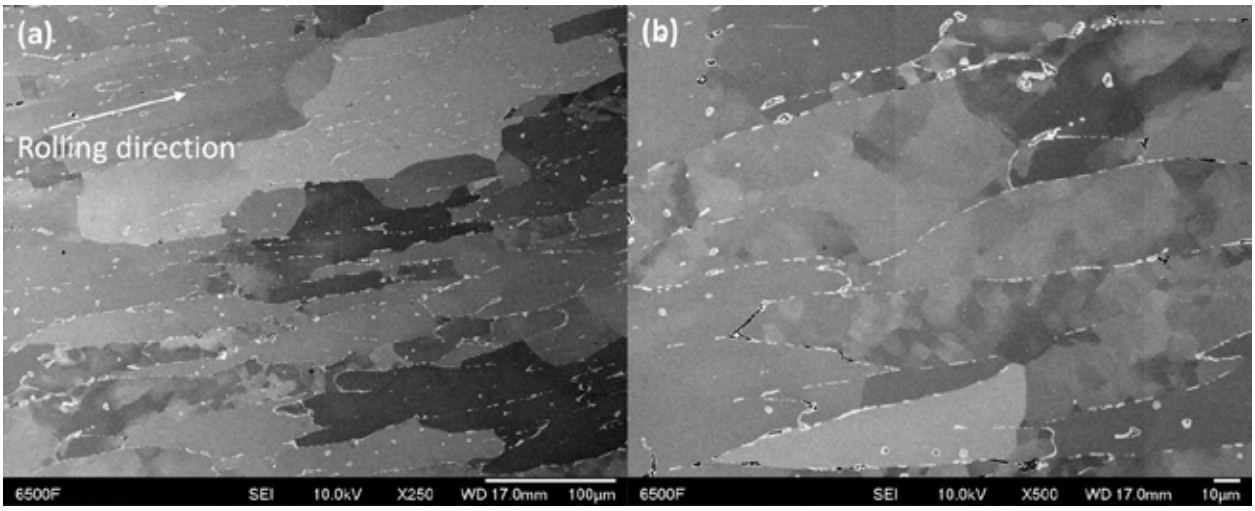

Figure 11. SEM images in different magnifications showing the grain structures in the rolled Z1N33A samples.

Figure 12a shows the fracture surface of the sample creep-ruptured at 650°C and 120 MPa in Figure 3a. Both dimple ductile and cleavage brittle features were observed. Figure 12b shows a higher magnification image of the ductile fracture from the center of the sample where the necking leads to the most surface area reduction. Dimples were observed with many of them having a core, identified to be Zr-rich and thus believed to be Laves phase precipitates. The dimples were formed as a result of voids nucleation at the cores and consequent voids growth and coalescence.

Figure 12c presents a higher magnification image of the brittle fracture area shown at the right part of Figure 12a. Both intragranular fracture and intergranular decohesion were noticed with the former being the dominant. Some circular features and river marks were observed on the plain surfaces of intragranular fractures, which were respectively marked by white and black triangles. The circular features are typically below 5 μm in diameter, which were later confirmed to be Laves phase by TEM. The precipitates found in the brittle fracture sites were in general larger compared to those presented in the ductile fractures. The presence of river marks indicates that multiple initial cracks propagated and joined to form the cleavage fracture.

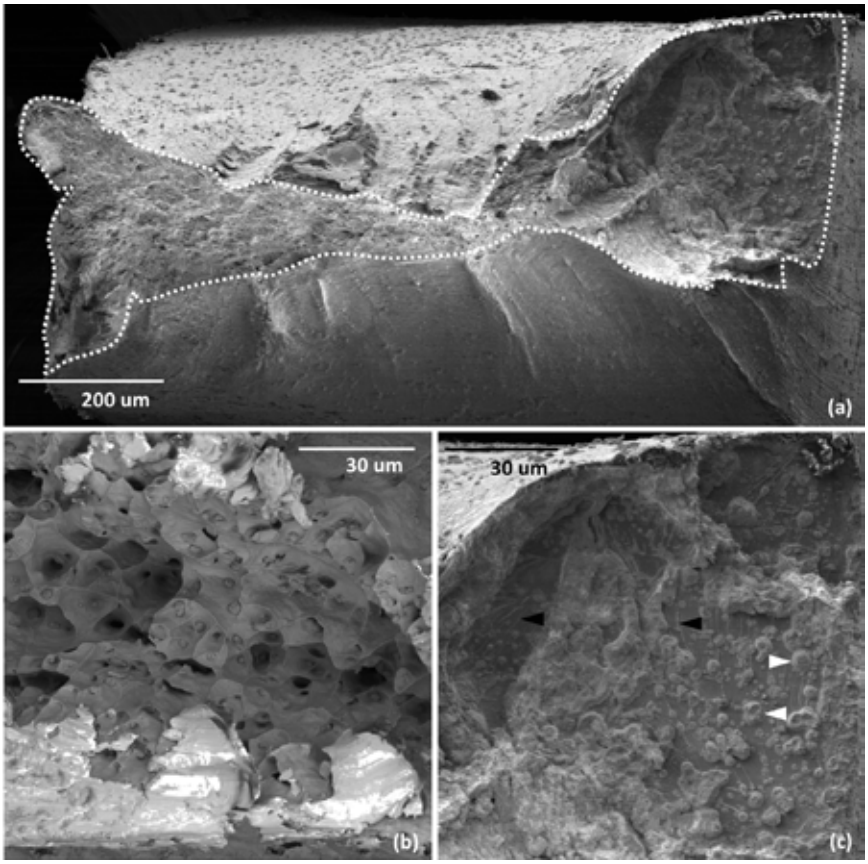

Figure 12. Overview of the (a) fracture surface and high magnification micrographs of the (b) ductile and (c) brittle regions of a Z1N33A sample creep tested at 650°C and 120 MPa.

Figure 13 shows the FIB lifted-out samples from the ductile and brittle fracture surfaces in (a) and (b), respectively. Before the samples were lifted-out, a protective Pt layer was deposited on the fracture surfaces schematically marked with the dotted lines in Figure 13. The ductile surface shows curvatures from the dimples, while the brittle surface has segments connected with steps, which are shown as the river marks in Figure 12c. As suggested by the creep curve in Figure 3a, the material underwent significant deformation in the tertiary creep stage. To accommodate the high strain and the necking, high density of dislocations formed and led to grain refinement as shown in Figure 13a. Such grain refinement was not observed underneath the brittle surfaces, indicating that the brittle fracture happened without undergoing the high-strain tertiary stage of creep.

The round particles in Figure 13b, pointed by white triangles, were evolved from Laves phase precipitates. Within the particles, EDS point surveys revealed that the regions having dark and bright contrast are respectively oxide of the matrix elements (Fe-Cr-O) and oxide of zirconium (Zr-O). Although detailed kinetics and dynamics of the Laves phase oxidation is beyond the scope of this study, it is believed that the Zr-O core was formed by inward diffusion of oxygen because of the higher affinity to oxygen of Zr. Particularly, the left particle shows an out shell of Fe-Cr-O and an inner core of Zr-O, indicating that decohesion might have occurred at the interface of the precipitate and the matrix during the creep test, providing channels for oxygen to react with the Laves phase from the interface. Figure 13b also shows cavities at the precipitate-matrix interface, suggesting that cracks could be initiated at and/or easily propagated through the interface between the coarse Laves phase precipitate and the matrix. The size of the

Laves phase is comparable to that primarily decorating grain boundaries in Figure 11, suggesting the detrimental effect of the coarse Laves phase.

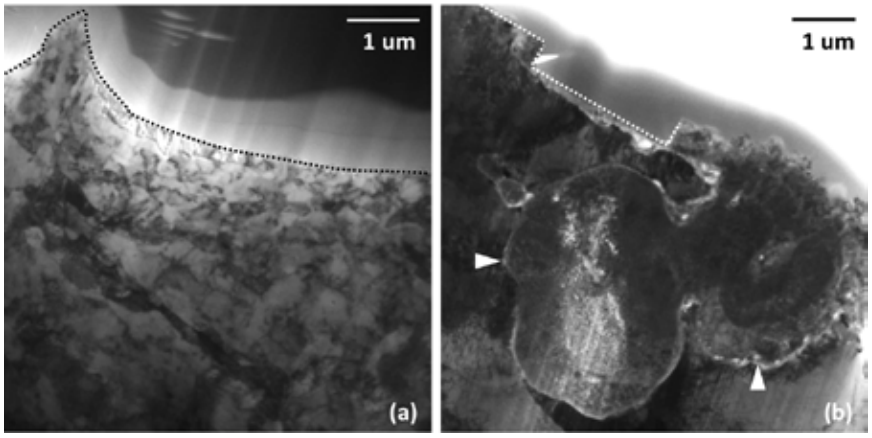

Figure 13. STEM micrographs of the creep-ruptured Z1N33A showing the regions near the (a) ductile (bright-field) and (b) brittle (HAADF) fracture surfaces.

Figure 14 reveals the dislocation-precipitate interaction observed at the brittle fracture site, where most deformation was believed to take place before the tertiary creep stage. In Figure 14a, a Laves phase precipitate, pointed by the black triangle, acted as an obstacle to dislocations. Dislocations were pinned and piled up at the precipitate-matrix interface, tending to increase the local stress at the interface. On the other hand, the finer NiAl precipitates, pointed by white triangles in Figure 14, were observed to exert an Orowan strengthening effect. In Figure 14a, some NiAl precipitates were observed to be surrounded by dislocation loops, resulted from a dislocation bypassing the precipitates through Orowan bowing, as exemplified in Figure 14b, pointed by a vertical white triangle. The mean diameter of the NiAl precipitates was increased to be 34 ± 10 nm with the density decreased to the order of 10^{14} cm^{-3} compared to the as-received condition.

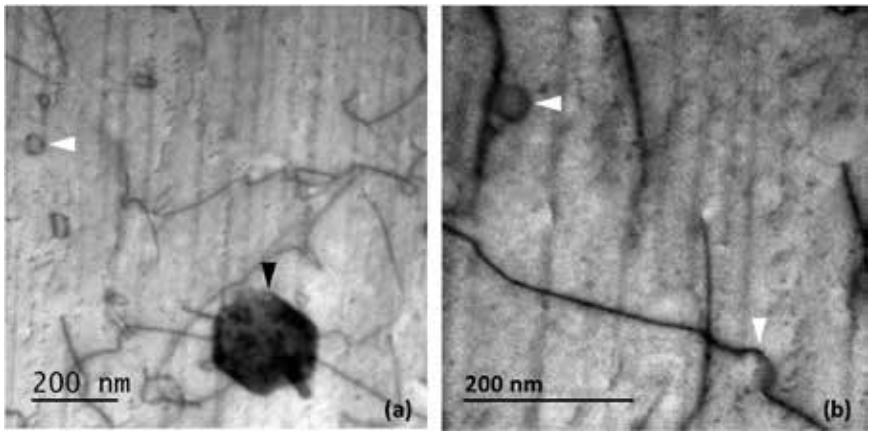

Figure 14. STEM bright-field micrographs of the creep-ruptured Z1N33A showing the interaction between dislocations and Laves phase and NiAl precipitates.

Figure 15 shows composition mappings, using EDS technique, obtained underneath the ductile fracture. Figure 15f and g indicate that most of the precipitates in the surveyed area were enriched in Ni and Al, which were further confirmed to be the NiAl B2 phase with SAD patterns. The average size of the B2 precipitates in this sample was found to be 42 ± 10 nm in diameter, tending to have an ellipsoid shape

elongated along the stress direction (which is the vertical direction in Figure 15). Coarsening of the B2 precipitates is more significant in the ductile site of the sample, suggesting that the higher level of strains during the tertiary stage may have enhanced the diffusion and thus accelerated the coarsening of the precipitates. Meanwhile, as observed in Figure 15e, a few fine Zr-rich precipitates were also present in the ductile site. Formation of the fine Laves phase during creep tests can also be a result of the enhanced diffusion under stress [8].

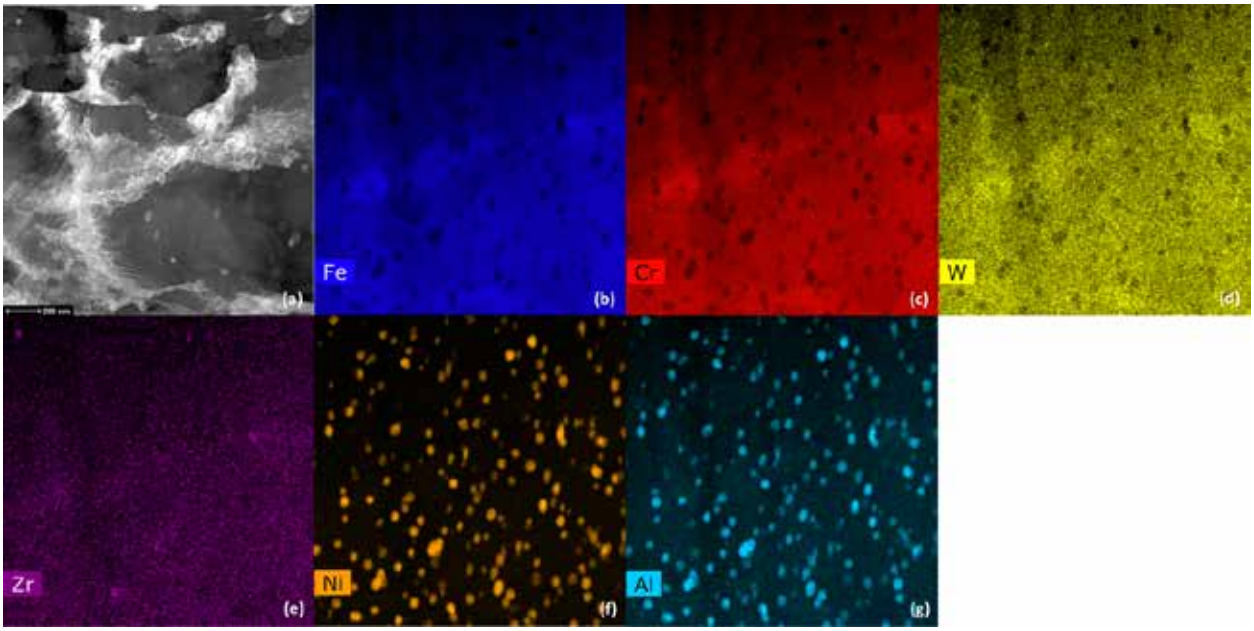

Figure 15. EDS mapping obtained near the fracture surface of the creep-ruptured Z1N33A, showing coarsening of B2 phase and suggesting formation of fine Laves phase.

The microstructure analysis of the Z1N33A sample after the creep test shows that the coherent B2 precipitates exert Orowan strengthening while the Laves phases precipitates pin dislocation and boundaries. During high temperature creep test, coarsening of the B2 precipitates deactivated the operation of Orowan strengthening. At the same time, fine precipitates of the Laves phase formed, which are believed to be able to immobilize dislocations. Coarse precipitates of the Laves phase, formed during alloy solidification, are detrimental to the high-temperature creep of the materials by initializing and promoting the propagation of cracks.

4.3. Alloys BL-Mo, BL-Nb and BL-NbZr

Backscattered electron images of the BL-Mo, BL-Nb, and BL-NbZr samples are shown in Figure 16a, b, and c, respectively. BL-Mo showed significantly larger grain size compared to the other two alloys. Coarse Laves phase was not observed in the BL-Mo, but in the BL-Nb and BL-NbZr samples. The coarse Laves phase is noticeably less than that in the Z1N33A sample in Figure 11. The minor Zr-alloying in the BL-NbZr tended to have elongated Laves phase compared to that in the BL-Nb. The high magnification images in the inset revealed dark fine particles in the BL-Mo, but white fine particles in the BL-Nb and BL-NbZr. According to the Z numbers of the alloy elements in the alloys, the dark fine particles in the BL-Mo are likely to be B2 NiAl phase, while the white fine particles in the BL-Nb and BL-NbZr are to be Nb/W/Zr-rich Laves phase. Laves phase in the BL-Mo is very limited, with the white particle in the inset of Figure 16a as an example.

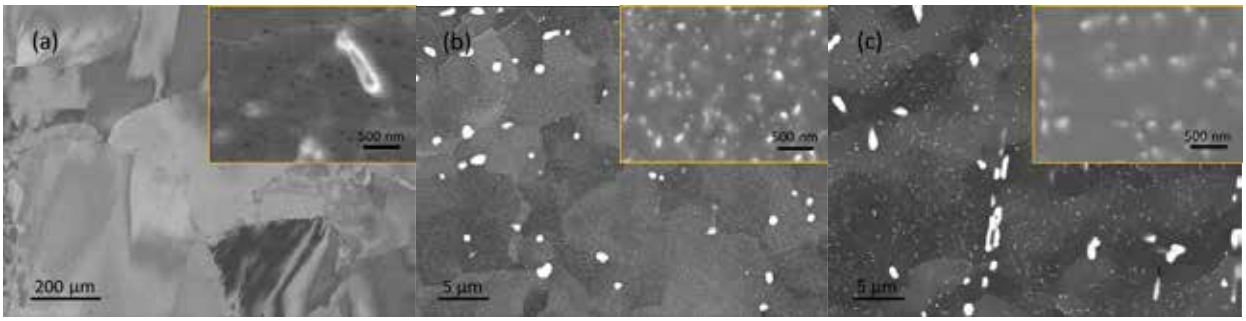

Figure 16. SEM images of (a) BL-Mo, (b) BL-Nb, and (c) BL-NbZr.

EDS spot mode was conducted on the BL-Mo sample. Examples of a coarse AlN inclusion and a fine Mo/Mn-rich particle (likely to be Fe_2Mo type Laves phase) are shown in Figure 17a-c and d-e, respectively.

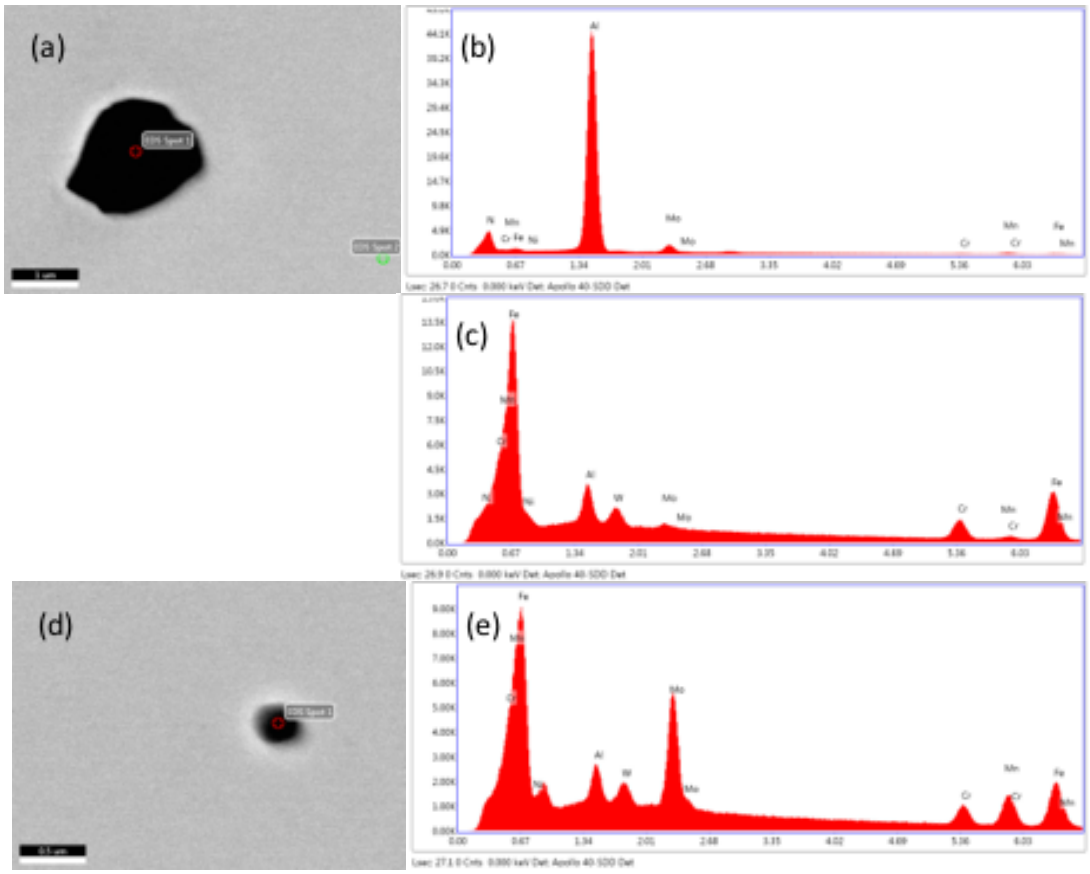

Figure 17. EDS spot analysis of BL-Mo indicating (a-c) a coarse AlN inclusions and matrix, as well as (d-e) a fine Mo/Mni-rich particle.

Figure 18a-c show the EDS mapping of the BL-Nb, indicating W/Nb-rich fine particles corresponding to the inset of Figure 16b. Similarly, Figure 18d-g show the EDS mapping of BL-NbZr showing W/Nb/Zr-rich coarse particles, but primarily W-rich fine particles.

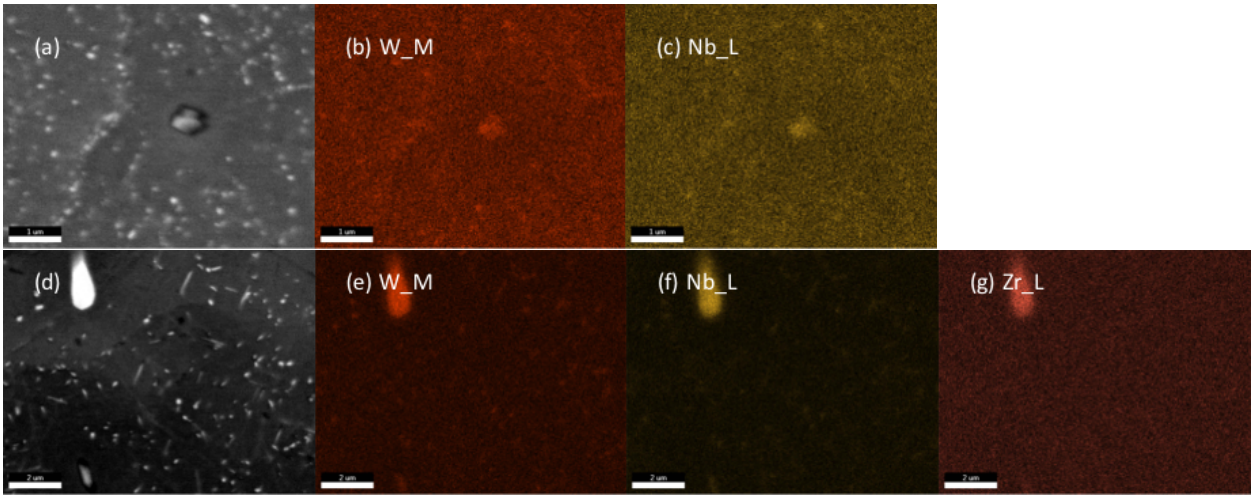

Figure 18. EDS mapping of (a-c) BL-Nb and (d-g) BL-NbZr showing the distribution of W, Nb and Zr in the coarse and fine precipitates.

Figure 19 shows the precipitate distribution in the BL-Mo sample. The SAD pattern in the inset of Figure 19a indicates that the precipitates taking a B2 structure are cubic-to-cubic coherent with the matrix. Dark-field micrograph imaged with the B2 reflection is shown in Figure 19b. Apparently there is a bimodal distribution of the precipitates, although both coarse and ultrafine precipitates have a coherent B2 structure enriched with Ni and Al (confirmed by EDS). The denudation of ultrafine precipitates around the coarse precipitates might suggest their similar chemical composition. According to the size and density, the coarse precipitates, with a size on the order of 50 nm, are likely to the those observed as dark particles under SEM in the inset of Figure 16a. The TEM-revealed ultrafine precipitates, with a size on the order of 10 nm, have a much higher density than the coarse precipitates. More studies are needed to understand the reasons of the bimodal distribution of the B2 precipitates. The BL-Mo did not exhibit good creep resistance in Figure 3a, which may be attributable to the low density of coarser particles because the finer particles tend to have smaller strength factor to resist deformation [9]. The effectiveness of such small precipitates (e.g., ~10 nm) on pinning dislocations needs to be investigated, comparing to that of the coarser precipitates (e.g., ~50 nm and larger).

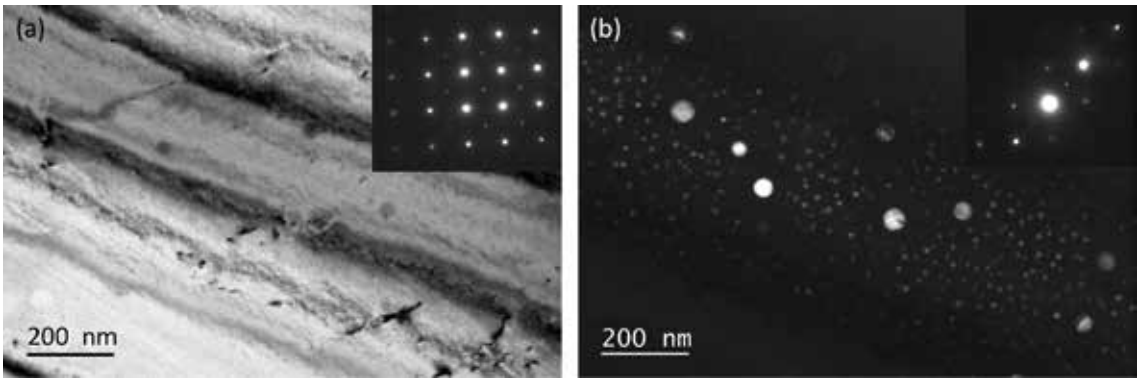

Figure 19. BF and DF TEM images showing the BL-Mo sample in which the coherent B2 precipitates having a bimodal distribution in size.

Figure 20 shows the microstructure of the BL-Nb sample. Precipitates of both Laves phase and B2 phase were observed in the TEM sample. Comparing to the bright-field image in Figure 20a, Figure 20b

shows the dark-field image obtained using the diffraction spot of the Laves phase. The inset SAD pattern of Figure 20b indicates that the Laves-phase precipitate is coherent with the {110} plane of the ferritic matrix. The size and density of the Laves phase are approximately consistent with the SEM-revealed Laves phase in the inset of Figure 16b. Figure 20c shows the dark-field image obtained using the reflection of the B2 phase. The inset SAD pattern of Figure 20c indicates a cubic-on-cubic coherency between the B2 phase and the matrix.

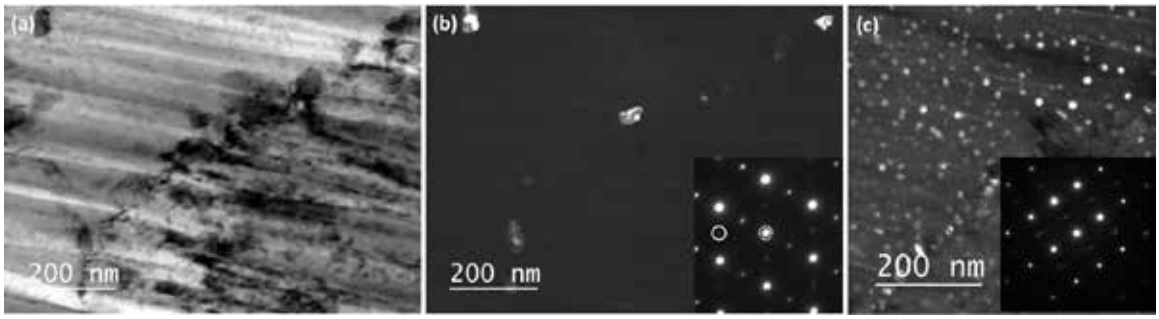

Figure 20. (a-b) BF and DF images showing the Laves phase in BL-Nb sample. (c) DF image showing the B2 precipitates.

Similarly, Figure 21 shows the microstructure of the BL-NbZr sample. The dark features in the bright-field micrographs in Figure 21a and b are the Laves-phase precipitates. Their chemical compositions were found to be $(Fe,Cr)_2(Zr,Nb,W)$ using EDS. Their crystal structures are found to be C14 Laves phase, based on the SAD pattern in the inset of Figure 21a, which further illustrate a coherency of $[10\text{-}10]_{Laves}//[113]_{Matrix}$ and $(0001)_{Laves}//(1\text{-}10)_{Matrix}$ between the Laves precipitate and the ferritic matrix. The morphology of the Laves-phase precipitates was influenced by the coherency relationship. In Figure 21a, the coherent edges of the precipitate are longer and sharper. Figure 21b further shows the effect of coherency on precipitate morphology. The precipitates were elongated along the direction within coherency plane. The Lave phase morphology changes might be influenced by the Zr alloying because such a morphology was not observed in the BL-Nb sample. The Ultrafine precipitates of B2 phase were also observed in the BL-NbZr sample, as shown in Figure 21c as the bright spherical features. The B2 precipitates the BL-NbZr have size and density similar to that in the BL-Nb in Figure 20c. However, the BL-NbZr exhibited creep resistance inferior to the BL-Nb as shown in Figure 3, which further suggests that the ultrafine B2 particles would not be a primary contributor the creep resistance. The B2 particles in the Z1N33A, which have a size about 3 times of that in the BL-Nb, BL-NbZr, and BL-Mo, showed Orowan mechanism when interacting with dislocations. Detailed dislocation-particle interaction studies will be pursued by comparing the different sizes of the particles in the BL-NbZr, BL-Nb, and BL-Mo, as well as the Z1N33A.

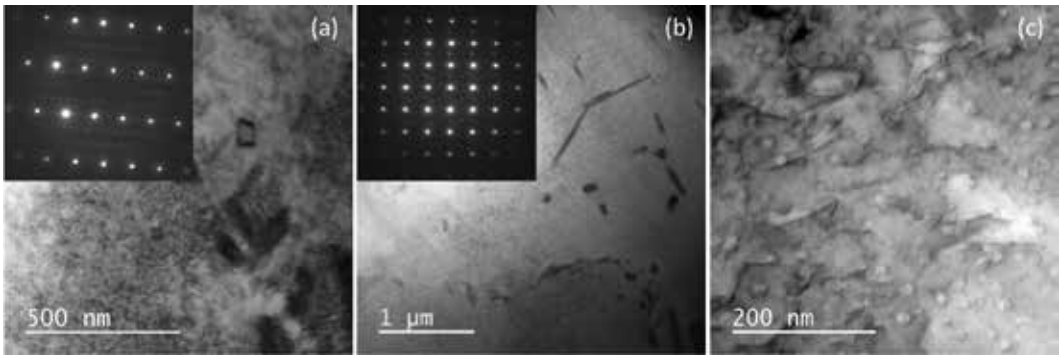

Figure 21. (a-b) STEM-BF micrographs showing the coherent Laves phase with the inset of SAD patterns indicating the precipitate-matrix orientation relationships and (c) B2 precipitates in BL-NbZr.

5. HEAVY ION IRRADIATION

Fe^{2+} ion irradiation was conducted at the ion beam lab, Universit of Wisconsin-Madison. The irradiation temperature was 475 °C and the nominal peak damage was 220 dpa with the ion energy being 4 MeV. Figure 22 shows the damage profile of 4.0 MeV Fe^{2+} irradiation in 79Fe-12Cr-3W-3Ni-3Al, the main composition of the alloys from BL-Nb to Z1N33A. To achieve a damage of 100 dpa at 0.48 μm where the damage profile is relatively flat (damage vs. depth slope is relatively small), a fluence of 2.14×10^{17} Fe^{2+}/cm^2 was used. The peak damage is 217 dpa at 1.1 μm under surface.

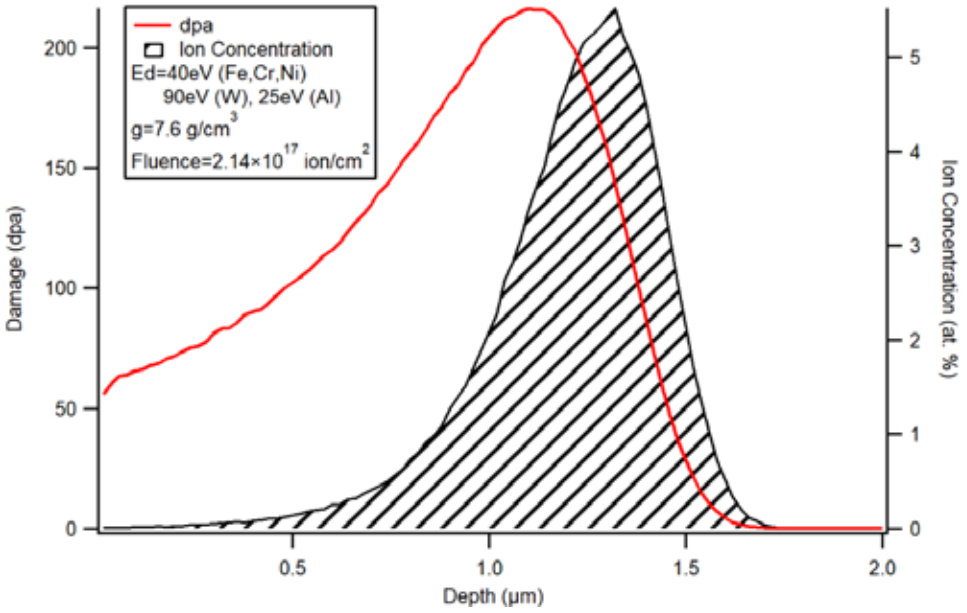

Figure 22. 4 MeV iron induced damage in 79Fe-12Cr-3W-3Ni-3Al, the main composition in wt% of alloys from BL-Nb to Z1N33A. The damage (unfilled) and implantation (filled with lines) profiles were calculated using the Kinchin-Pease model in the Stopping and Range of Ions in Mater (SRIM) software. *Ed* is atom displacement energy.

Irradiation temperature and flux are shown in Figure 23. Temperature is average value of two thermocouple readings from opposite corners of the sample stage. Flux was calculated from ion beam current and beam scanning area (2 cm^2). Occasional positive or negative flux spikes resulted from spikes of ion current or possibly secondary electron currents. In run 1, temperature is 474 ± 3 °C and flux is (6.4 ± 0.8) × 10^{12} ion/cm^2/s. In run 2, temperature is 472 ± 2 °C and flux is (6.6 ± 0.9) × 10^{12} ion/cm^2/s. The sample ID used in the irradiation part of work, with Nb2-1 as an example, denotes the 2nd batch sample BL-Nb2 with 1-step heat treatment in contrast to the 1st batch sample BL-Nb1 with 2-step heat treatment after the 1st run (-1) of irradiation experiment differentiating from the 2nd run (-2) irradiation.

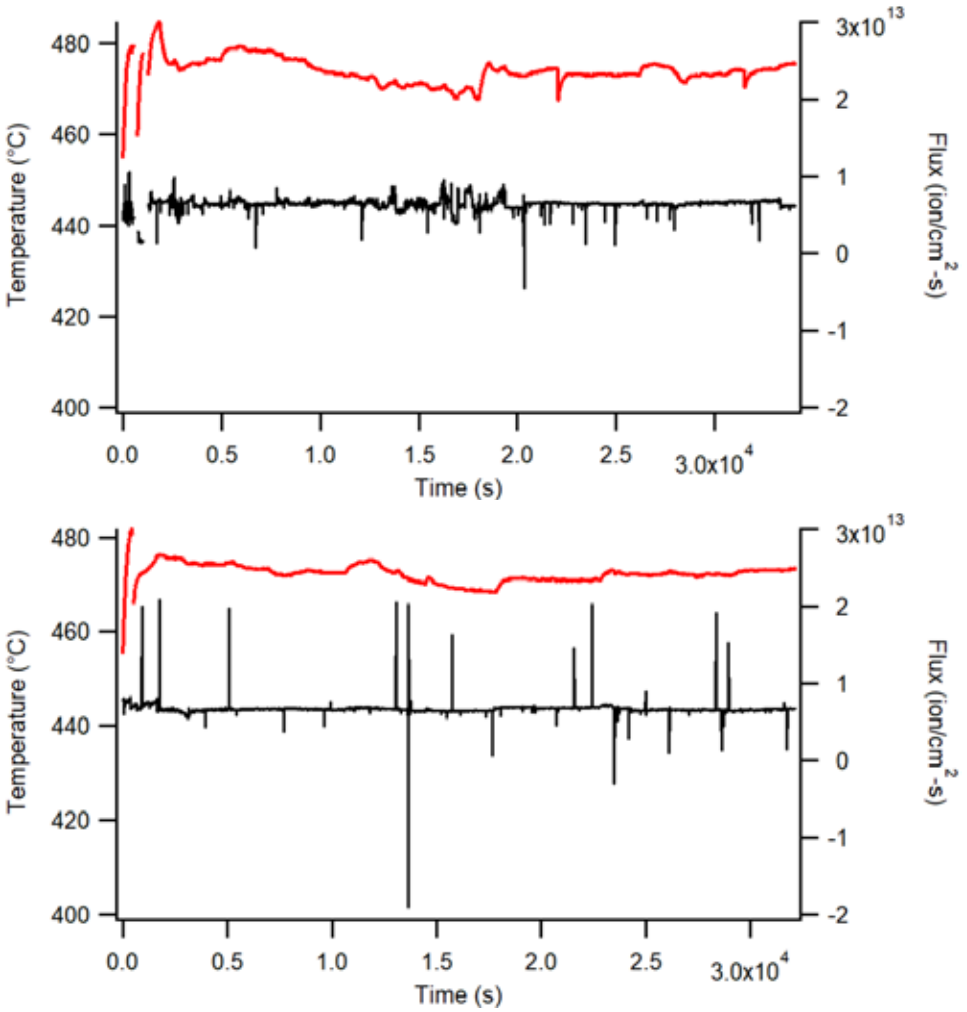

Figure 23. Temperature (red lines) and flux (black lines) during 4 MeV iron irradiation. (top) 1st run irradiation: Nb1-1, Nb2-1, NbZr1-1, NbZr2-1, Mo1-1, Mo2-1, TTZ2M-1 and Z1N33A-1. (bottom) 2nd run irradiation: Nb1-2, Nb2-2, NbZr1-2, NbZr2-2, Mo1-2, Mo2-2, 53T1-2 and 63T1-2.

5.1. Radiation-induced surface changes

Figure 24 shows photographs of samples after Fe^{2+} ion irradiation at 475 °C up to 220 dpa. Samples were partially masked so that the masked region did not receive any irradiation but experienced similar thermal history as the irradiated region. The irradiated areas turned brown possibly due to mild oxidation while unirradiated parts are of silver color. Among the irradiated samples, 53T1-2 and 63T1-2 were not focus of this work.

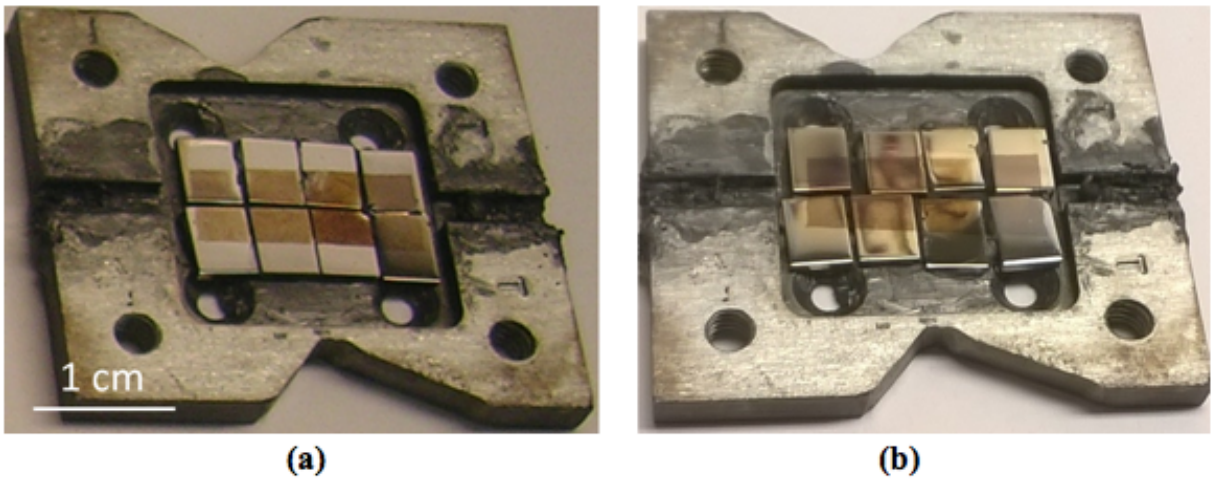

Figure 24. Samples after 475°C, 200 dpa Fe^{2+} ion irradiation. (a) 1st Run: the samples from left to right are Nb1-1, NbZr1-1, Mo1-1, TTZ2M-2 (first row), Nb2-1, NbZr2-1, Mo2-1, Z1N33A-2 (second row); (b) 2nd Run: the samples from left to right are Nb1-2, NbZr1-2, Mo1-2, 53T1-2 (first row), Nb2-2, NbZr2-2, Mo2-2, 63T1-2 (second row). Samples are identified with alloy labels and a number system referring to irradiation runs.

If irradiation induced swelling, surface of unirradiated region will be higher than irradiated region. Sample height around the irradiation boundary were measured with Zygo New View 6000, a white light interferometer. Figure 25a shows a height map of a 53T1-2 sample irradiated with Fe^{2+} up to 220 dpa at 475 °C. An irradiation boundary lies vertically along x=180 μm in Figure 25a. Irradiated part is at left. Figure 25b displays the average height of all y pixels in figure 1a against x coordinates. Up to ten images consisting of 3.1×10^6 pixels with a total area of 0.92 mm^2 were acquired. Height background was removed using polynomial degree of two to keep unirradiated area flat.

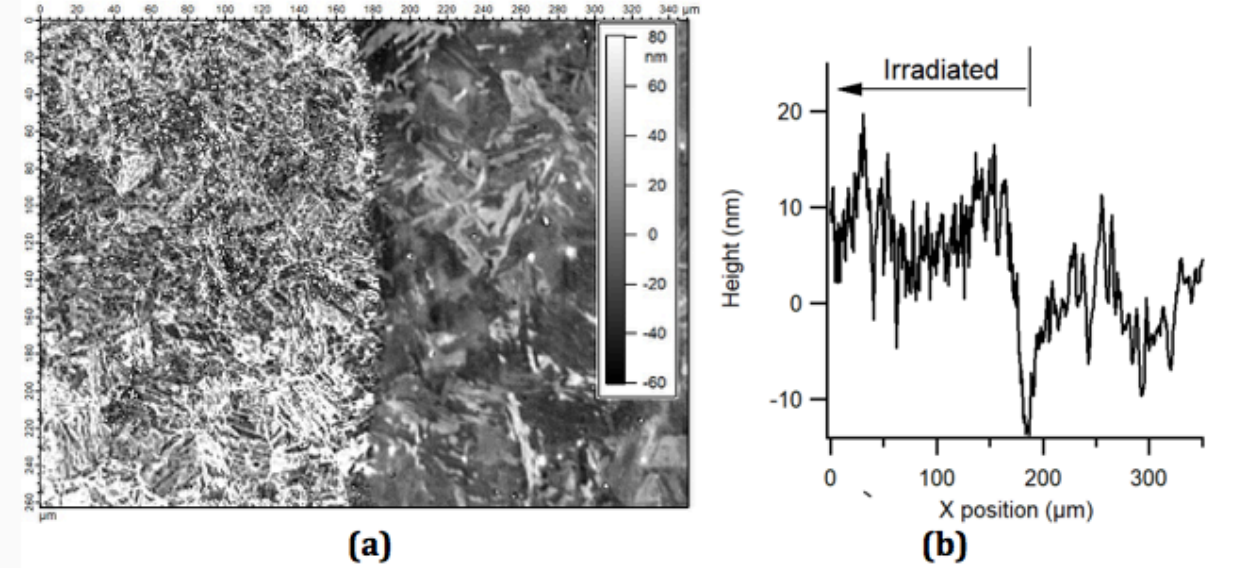

Figure 25. Optical profiling measurement of Fe^{2+}-irradiated 53T1-2 sample up to 220 dpa at 475 °C. (a) Height map. Irradiation boundary is a vertical line at x=180 μm. Sample at left was irradiated. (b) Average height along x position.

Assuming surface oxide does not reflect light, the measured step height is height difference at metal/oxide interfaces in irradiated and unirradiated area. Table 3 lists the results of optical profiling.

Table 3. Step height differences between unirradiated and irradiated regions after Fe^{2+} ion irradiation at 220 dpa 475 °C.

Sample label	Average heights (nm)		Height of irradiated surface above unirradiated (nm)
	Irradiated	Unirradiated	
53T1-2	6.85 ± 0.04	-0.32 ± 0.02	7.17 ± 0.06
63T1-2	22.5 ± 0.1	-0.17 ± 0.05	22.6 ± 0.2
Nb1-1	0.56 ± 0.09	0.89 ± 0.04	-0.3 ± 0.1
Nb2-1	12.57 ± 0.05	1.51 ± 0.02	11.05 ± 0.07
NbZr1-1	-1.90 ± 0.05	0.90 ± 0.02	-2.79 ± 0.07
NbZr2-1	-16.69 ± 0.04	0.44 ± 0.02	-17.13 ± 0.06
Mo1-1	-89.53 ± 0.06	-0.30 ± 0.01	-89.24 ± 0.07
Mo1-2	18.55 ± 0.05	1.73 ± 0.03	16.82 ± 0.08
Mo2-1	53.50 ± 0.04	3.28 ± 0.02	50.23 ± 0.06
Mo2-2	1.48 ± 0.03	1.62 ± 0.02	-0.15 ± 0.05

Table 3 shows large variation of step heights on the same materials irradiated separately yet under the same nominal conditions. Mo1-1 and Mo1-2 are Mo1 alloys irradiated during the first and second irradiation run, respectively. The step heights are about -89 nm on Mo1-1, and about 17 nm on Mo1-2. For Mo2 alloy, step heights are 50 nm on Mo2-1 and nearly 0 on Mo2-2. Figure 26 shows the optical height images of Mo1-1 (a) and Mo2-1 (b). There are scratches from sample polishing in both images. The irradiated region in Mo1-1 (Figure 26a) shows some scratches that are invisible in the unirradiated region. It indicates that irradiation eroded surface and exposed deeper scratches. On the contrary scratches in the irradiated and unirradiated regions of Mo2-1 (Figure 26b) are similar.

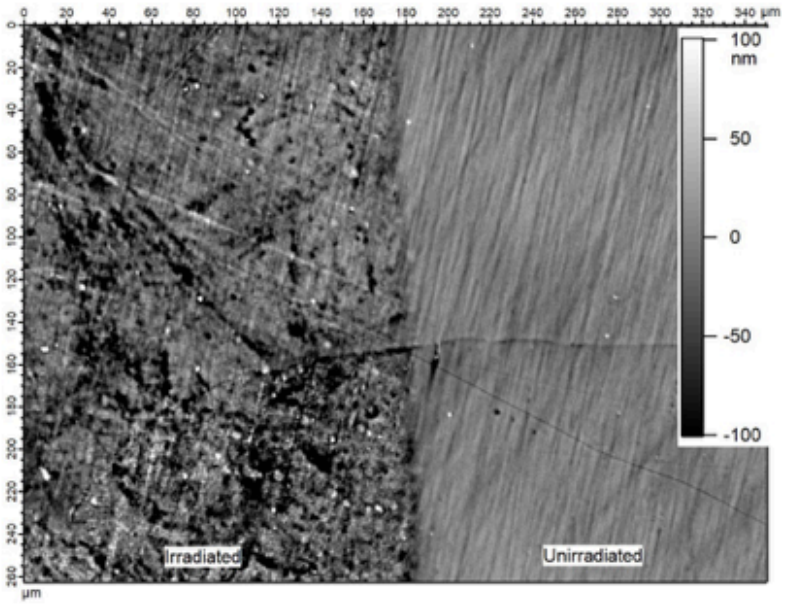

(a)

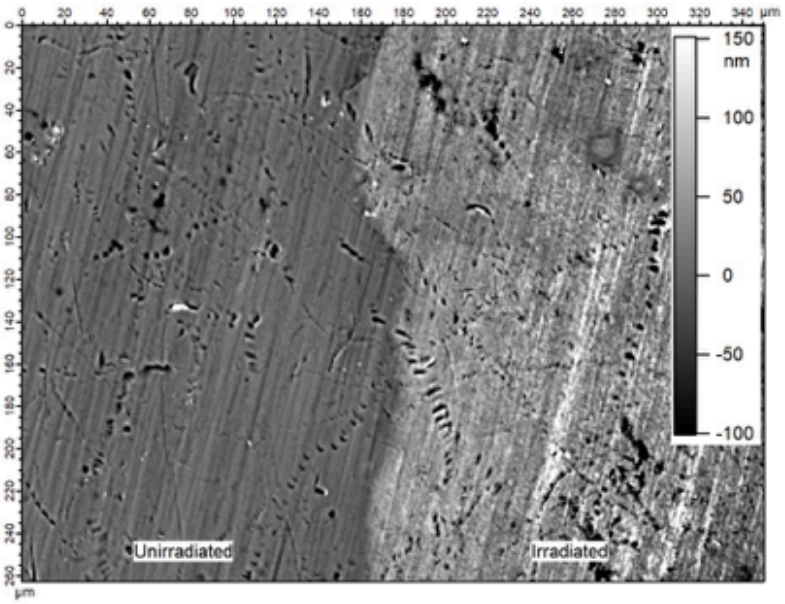

(b)

Figure 26. Optical topography images of samples: (a) Mo1-1, (b) Mo2-1.

Swelling would result in positive step height (irradiated surface height above unirradiated surface). However, ion sputtering would lead to a loss of material and hence a recession of the irradiated surface. Likewise, oxidation would reduce metal mass but increase the height of the sample surfaces assuming the general outward diffusion of iron during oxidation. All these factors should be considered while evaluating swelling.

Loss of atoms by sputtering is estimated with a sputtering yield of 2 atoms/ion, calculated from an empirical equation assuming sputtering yield of 4 MeV ions the same as 1 MeV [10]. Ion fluence was 2.14×10^{17} ion/cm^2. Sample thickness reduction due to sputtering is calculated as $t = nM/(N_A\,\rho)$, where n

is number of sputtered atoms (4.28×10^{17} atom/cm^2), M is molecular mass of steel (56 g/mol), N_A is Avogadro's number (6.02×10^{23} /mol), and ρ is density (8 g/cm^3). The result is 50 nm. As ion beam rastered through samples, atom loss due to sputtering is expected to be about the same for all samples.

Figure 27a-c show secondary electron images of irradiated surface of Nb1-1, NbZr1-1, and Mo1-1, respectively, indicating irradiation-induced oxidation on the samples. The spherical and elongated globular structures are oxides. It appears that oxides cover a larger surface area on Mo1-1 than that on Nb1-1 and NbZr1-1.

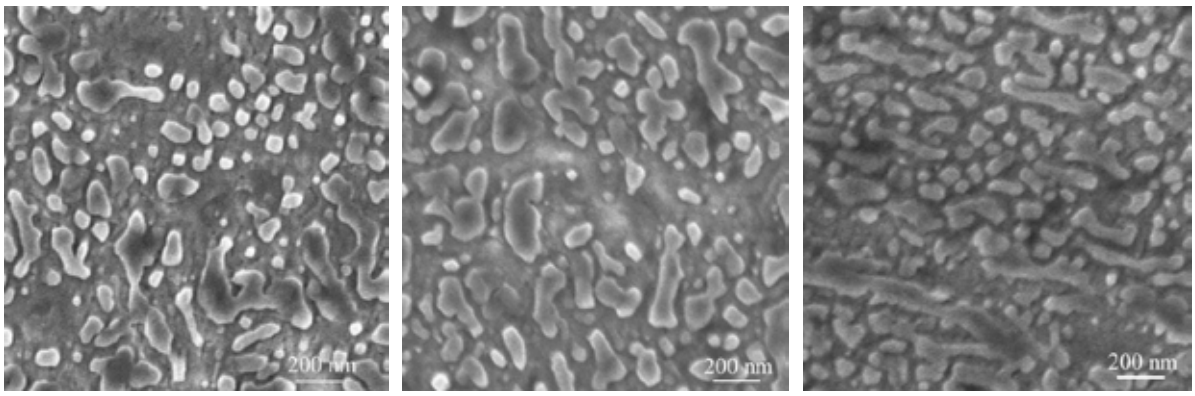

(a) **(b)** **(c)**

Figure 27. Secondary electron images of samples irradiated with Fe^{2+} up to 220 dpa at 475 °C: (a) Nb1-1, (b) NbZr1-1, (c) Mo1-1. Electron beam energy was 3 kV.

It is estimated that 4.5 nm thick steel transforms to 10 nm thick Cr_2O3 or Fe_2O_3, using density of oxides (5.2 g/cm^3) and density of steel (~ 8 g/cm^3). The height increase of the samples due to oxidation is similar for Nb1-1 and NbZr1-1, but may be larger for Mo1-1.

Optical profiling result shows lower irradiated surfaces in Nb1, NbZr1, Mo1 than 53T1 and 63T1. To accurately determine swelling using step heights at irradiation boundary, we need to systematically quantify the oxidation, sputtering and other factors.

5.2. Post-ion-irradiation microstructure characterizations

Figure 28 shows cross-sectional TEM and scanning-TEM (STEM) images of Nb1-1. Precipitates (~ 100 nm to several microns in size) are present both along grain boundary and in grains. In addition, smaller spherical particles ~ 15 nm are observed inside the grains. Figure 28c-d show a large particle and the diffraction pattern. Diffraction spots from the particle are indicated by red dots. The interplanar distances for the particle phases are 0.77 nm and 0.42 nm, close to Laves phase Fe_2Nb {001}, {100}, respectively. Irradiation generated dislocations and dislocation loops in a 1.2 μm deep surface damaged layer, as shown in Figure 28e-f. Figure 28g shows large particles ~ 100 nm near the end of damage range. However, in the irradiated region, these particles experienced considerable damage in the form of disintegration. Additionally, inside the damaged zone structures ~ 10 nm or smaller were observed, as shown in Figure 28h.

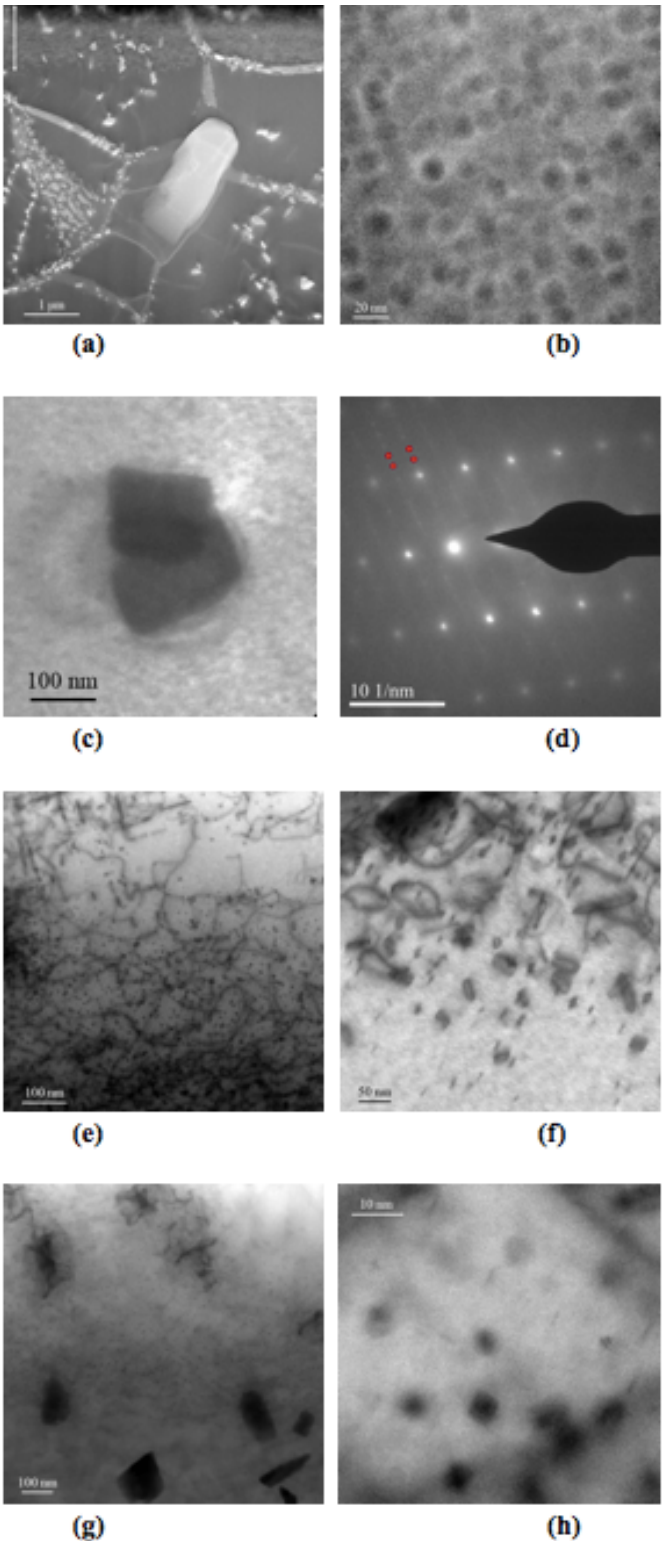

Figure 28. Cross-sectional STEM and TEM images of Nb1-1 irradiated with Fe^{2+} up to 220 dpa at 475 °C. (a) High angle annular dark field image. Arrow indicates the irradiation damage layer. (b) HAADF image of undamaged area. (c) Bright field image. (d) Electron diffraction pattern of area in (c). (e-h) Annular bright field images of damaged layer. Sample was orientated not along a zone axis in (a, b, g), along <311> in (c, d) and along <100> in (e, f, h).

Composition of precipitate particles in alloy Nb1-1 was measured with EDS in the TEM. Figure 29a-b show composition of larger precipitate to be close to $(FeCr)_2(NbW)$, confirming electron diffraction result (Figure 28d). Figure 29a also shows a contrast boundary in the $(FeCr)_2(NbW)$ particle, indicated by an arrow. Upper part of the particle was irradiated and turned into amorphous. Figure 29c-d show the spherical particles ~ 15 nm in size in undamaged region of the alloy and are possibly NiAl intermetallic phase. In damaged Nb1-1, the precipitates ~ 10 nm in size appear to be deficient in Al and Ni, as shown in Figure 29e-f. Figure 29g-i show a precipitate composition approximating $(AlNb)(CN)_x$ in the damaged region.

Figure 30 shows TEM images of NbZr1-1 irradiated with Fe^{2+} ions up to 220 dpa at 475 °C. As in the case of alloy Nb1-1, precipitates ~ 100 nm to several microns large are found both at grain boundary and inside grains, as shown in Figure 30a. The diffraction pattern from the particle in Figure 30b is shown in Figure 30c. The interplanar distance is 0.41 nm, corresponding to Laves phase Fe_2Nb (001) interplanar distance. The diffraction pattern matches with hexagonal lattice Fe_2Nb [001] zone diffraction. Figure 30d is a dark field image taken along matrix <211> zone (Figure 30e) upper panel). Secondary phase diffractions are represented by fine spots. The phase is of B2 order with lattice parameter close to BCC Fe (0.287 nm) suggesting that it could be the AlNi phase which also has a BCC B2 structure and has a lattice parameter of 0.288 nm. Irradiation produced dislocation network and dislocation loops, and appear to break down precipitates, as shown in Figure 30f. Figure 30g shows dislocation loops and/or small precipitates of size ~ 10 nm.

Figure 31 shows EDS characterization of precipitates in the damaged layer of NbZr1-1. The particles ~ 100 nm or larger are $(FeCrNi)_2(NbWZr)$ Laves phase, as shown in Figure 31a-d. Irradiation appears to have disintegrated the Laves phase particles from periphery. The W atoms distribute at a broader area around the remaining particle while Nb, Ni, Cr, Fe atoms are at core. Figure 31e-f show AlNi particles ~ 20 nm large. These particles were found in both damaged and undamaged NbZr1-1.

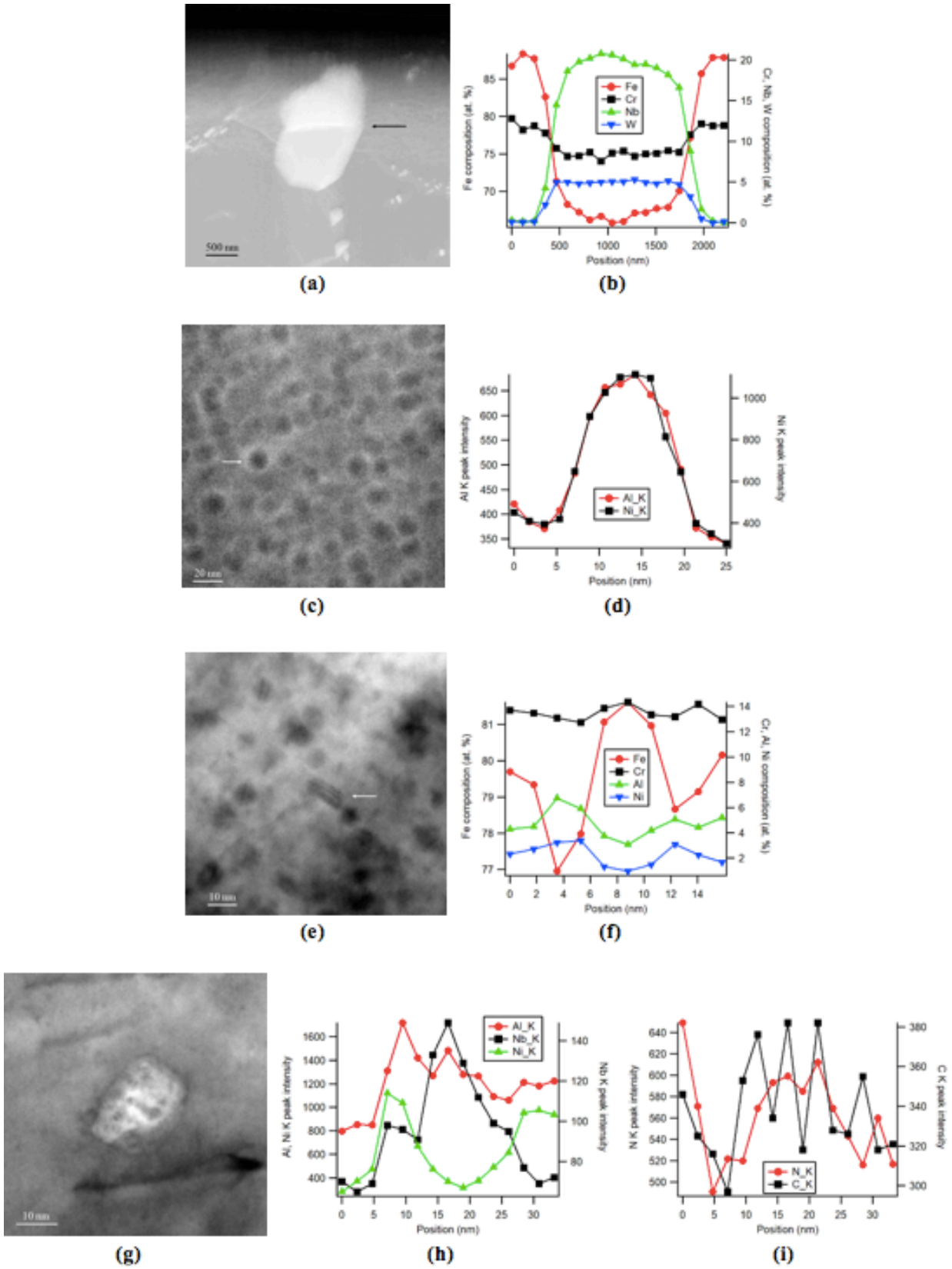

Figure 29. EDS analysis of particles in Nb1-1 irradiated with Fe^{2+} up to 220 dpa at 475 °C. (a, c) HAADF images. (e, g) ABF images. (b, f) Composition and (d, h, i) EDS peak intensity on particles in left images.

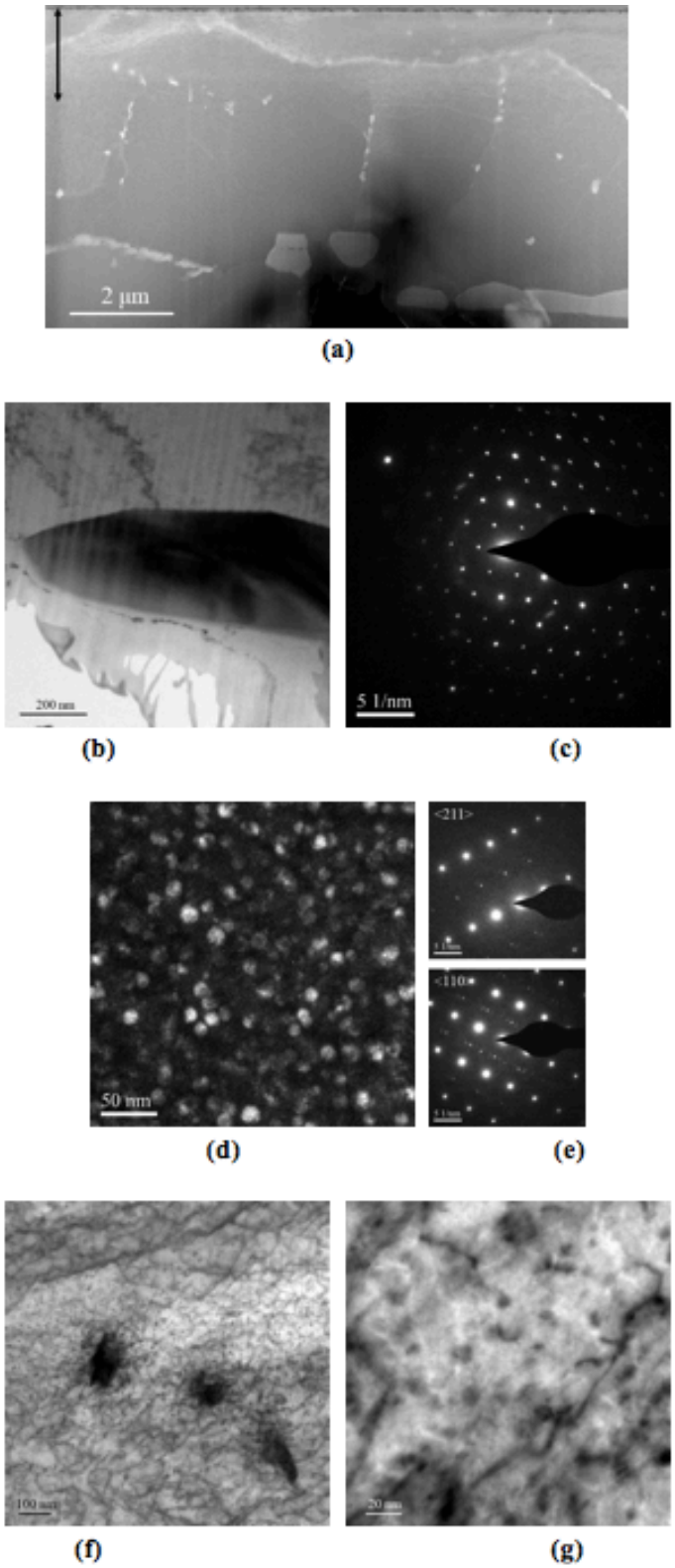

Figure 30. TEM images of cross sectional NbZr1-1 irradiated with Fe^{2+} ion up to 220 dpa at 475 °C. (a) HAADF image along <110> zone. Arrow indicates the damaged layer. (b) BF image of a large particle. (c) Electron diffraction pattern of the particle in (b). (d) DF image with the diffraction condition of (e, <211> zone). (f, g) ABF images of damaged area along <110> zone.

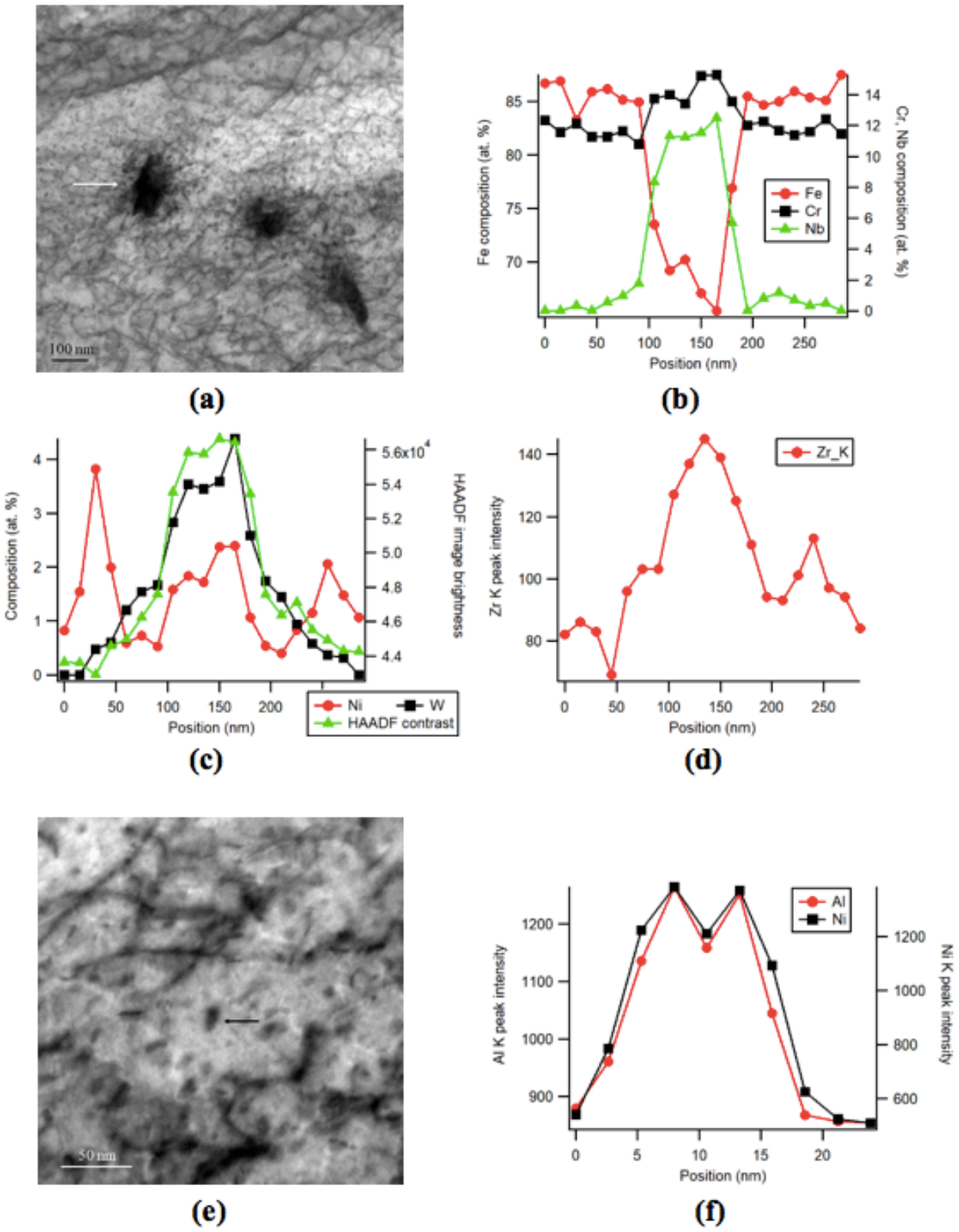

Figure 31. Compositional analysis of particles in NbZr1-1. (a, e): ABF images of damaged area. (b, c, d) and (f): Composition or EDS peak intensity profiles of the particles in (a), (e), respectively. The particles are indicated by arrow.

Sample Mo1-1 irradiated with Fe^{2+} up to 220 dpa at 475 °C has been studied with STEM. Figure 32 shows images of Mo1-1. Figure 32a shows irradiation damage in Mo1-1. The damaged layer is indicated by arrow. Irradiation produced dislocation networks and dislocation loops. There appear no voids. Figure 32b-c show elongated precipitates in the damaged region. Their size ranges from a few nanometers to tens of nanometers. Figure 32d shows spherical precipitates in undamaged Mo1-1. Most of the precipitates are between 10 nm to 20 nm in size, while some are about 50 nm large.

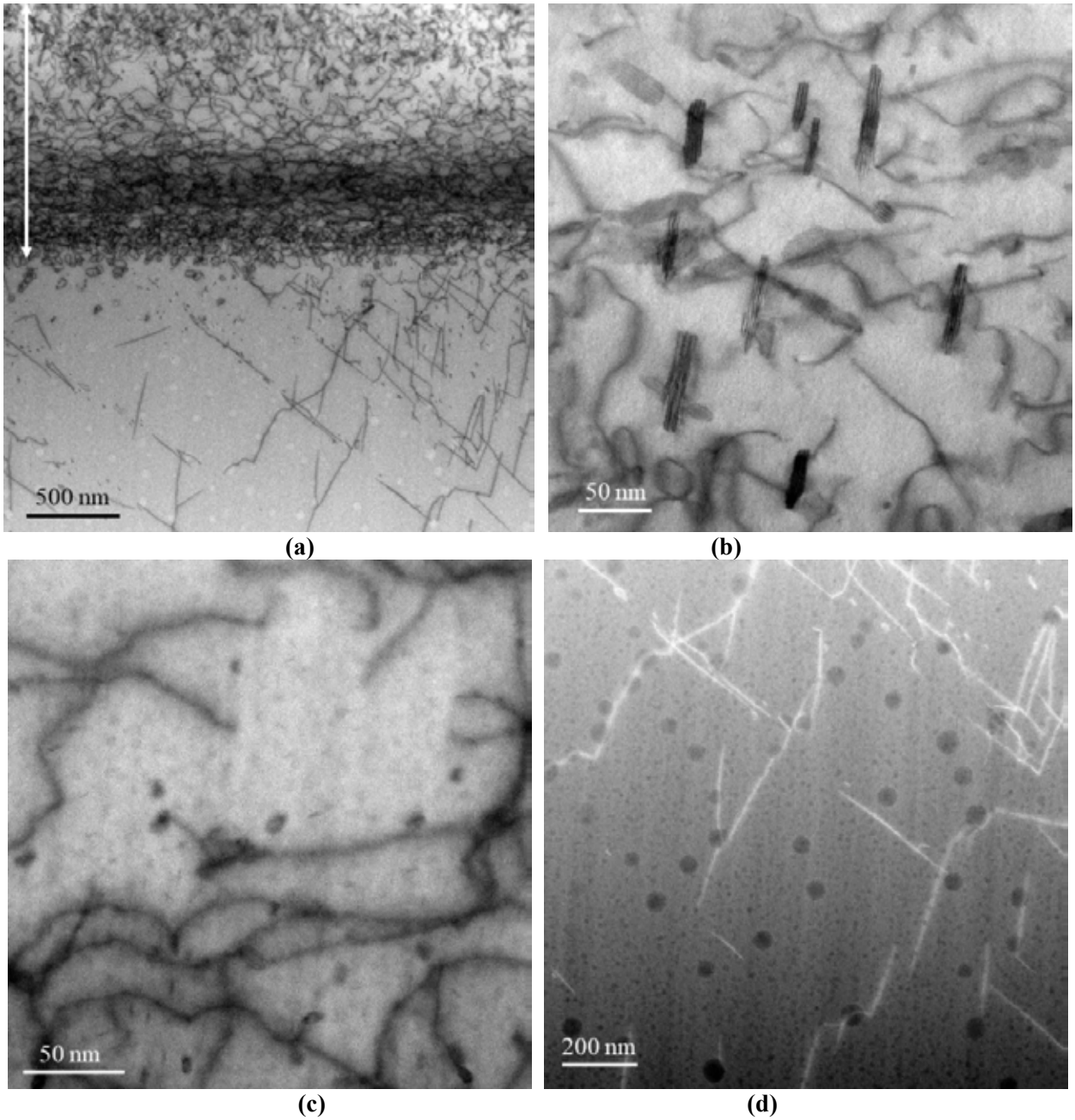

Figure 32. STEM cross-sectional images of Mo1-1 irradiated with Fe^{2+} to 220 dpa at 475 °C along <111> zone. (a-c): Annular bright field images; (d) high angle annular dark field image.

Figure 33 shows compositional analysis result of precipitates by energy dispersive x-ray spectroscopy (EDS). Two kinds of precipitates were found in Mo1-1: AlNi(CN)-rich precipitates in both undamaged and damaged region, and CrMo(CNO) particles in damaged region only.

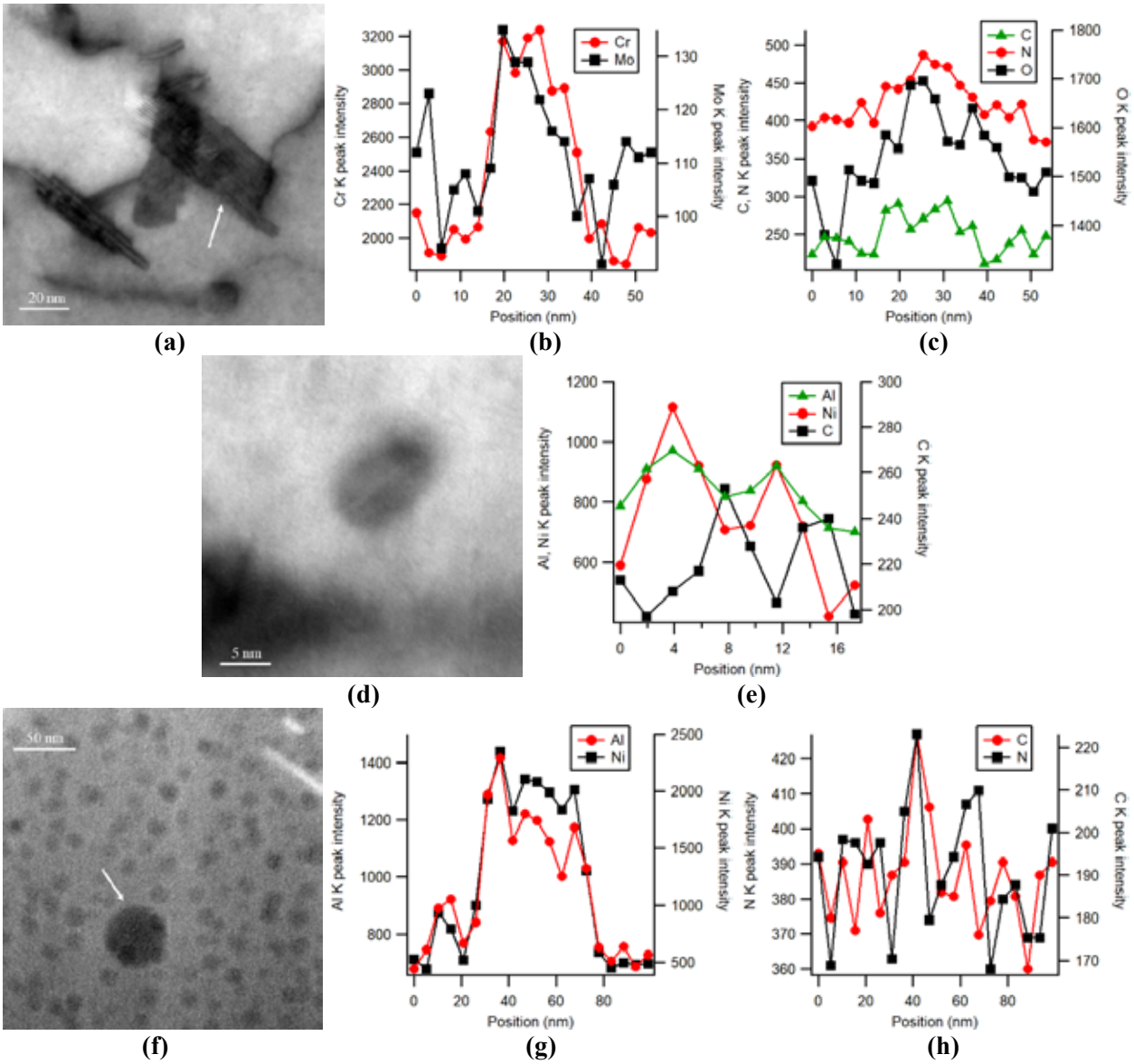

Figure 33. Compositional analysis of precipitates in Mo1-1. (a, d): annular bright field images in ion irradiation damaged region. (f): high angle annular dark field image in undamaged region. (b, c), (e), (g, h): EDS peak intensity profiles of the particles on (a), (d), (f), respectively.

Results of TEM characterization of Nb1-1, NbZr1-1 and Mo1-1 are summarized in Table 4. Up to a peak dpa of 220 dpa at 475 ºC, there is no void formation in any of the three alloys. In contrast, a number of voids with 24 ± 9.58 nm diameter and 6.8×10^{19} m^{-3} concentration were observed in T91 irradiated up to 250 dpa at 475 °C [11]. The B2 phase appears to be stable under irradiation, whereas the Laves phase underwent amorphization and disintegration as a result of irradiation.

Table 4. Microstructures of stainless steel samples irradiated with Fe^{2+} up to 220 dpa at 475 °C.

Sample	Precipitates in undamaged region	Irradiation damaged region	
		Precipitates	Dislocations or voids
Nb1-1	AlNi; $(FeCr)_2(NbW)$: ~ 100 nm to microns	AlNi; $(FeCr)_2(NbW)$: amorphized or disintegrated	Dislocations, dislocation loops, no voids
NbZr1-1	AlNi; $(FeCrNi)_2(NbWZr)$	AlNi; $(FeCrNi)_2(NbWZr)$: disintegrated	Dislocations, dislocation loops, no voids
Mo1-1	AlNi: spherical, ~ 20 nm	AlNi; $(CrMo)_x(CN)_y$: elongated, tens of nm	Dislocations, dislocation loops, no voids

5.3. Radiation induced nanomechanical changes

Samples irradiated with Fe^{2+} up to 220 dpa at 475 °C were measured using a Hysitron TI-950 TriboIndenter with a Berkovich tip and a High Load transducer. We have used two sample mounting methods. One is magnetic attachment. It resulted in unrealistically low modulus under high load. The reason may be sample moving under high force. The new mounting method is to glue the samples on 15 mm diameter metal discs (stainless steel alloy 430, Ted Pella Inc). Samples and discs were then glued on high-load stage. Indents were performed in displacement-controlled mode.

Indent area after tip retrieval is reported close to or the same as the indent area at max load [12]. Area function was calibrated using the SEM-measured projected indent area, A, on a stainless-steel sample (alloy 709) and contact displacement h_c, defined as $h_c = h_{max} - \varepsilon \times P_{max} / S$, where h_{max} is maximum displacement, ε is a geometric constant accounting for deflection of surface at contact perimeter, P_{max} is peak load, and stiffness $S = dP/dh$ is the slope of unloading curve. Figure 34 shows the relationship between A and h_c of 50 indents with displacements 0.5 – 2.5 µm. Fitting was performed with a 3rd order polynomial equation, $A = k_0 + k_1 h_c + k_2 h_c^2$. Within the displacement range 0.5 – 2.5 µm, indent area of all samples was calculated using the fitting equation and parameters.

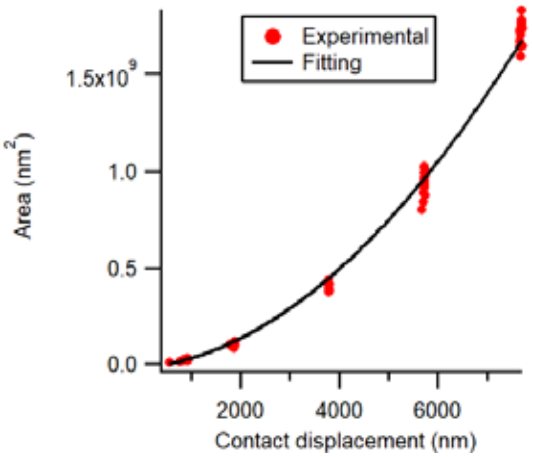

Figure 34. Indent tip area function calibration.

Ten indentation measurements were performed at the two displacements of 1 and 2 μm. Figure 35 shows hardness results of (a-b) BL-Nb, (c-d) BL-NbZr, (e-f) BL-Mo, (g) Z1N33A measured at the University of Wisconsin-Madison, and (h) TTZ2M-2 measured at Oak Ridge National Laboratory.

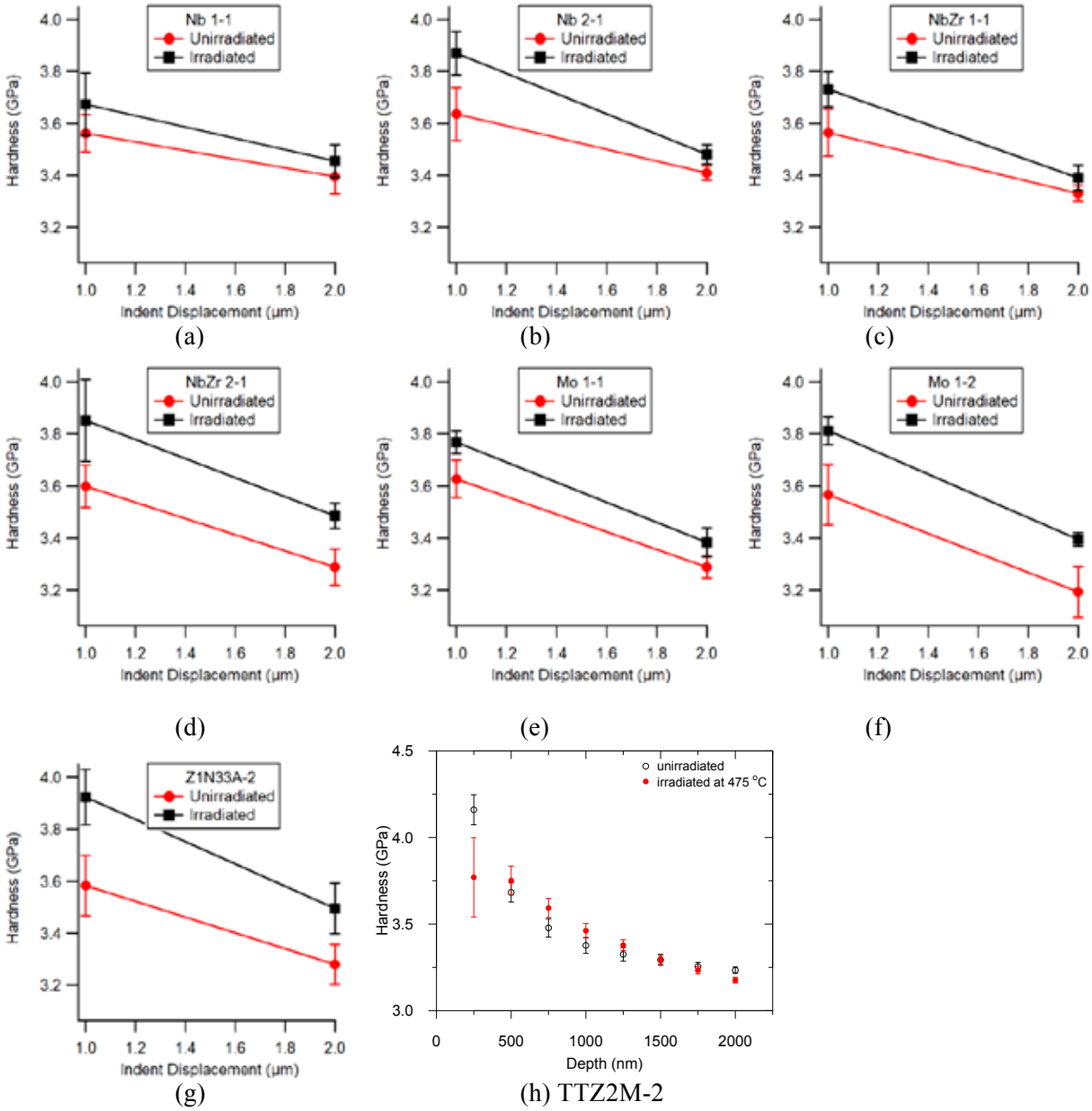

Figure 35. Nanohardness as function of indent displacements for eight samples at the irradiated (up to 220 dpa at 475°C) and unirradiated surfaces.

Elastic modulus (E) were measured during the nanoindentation, assuming Poisson's ratio of steel is 0.3. Modulus results in the unirradiated and irradiated conditions at 1 and 2 μm depth, together with their changes (ΔE), are summarized in Table 5. The modulus values range from ~188 to ~239 GPa. The irradiation generally resulted in slightly lower modulus or negligible changes.

Table 5. Nanoindentation-measured elastic modulus of samples irradiated with Fe^{2+} up to 220 dpa at 475 °C.

	Modulus (E, GPa) at 1 μm			Modulus (E, GPa) at 2 μm		
	Unirradiated	Irradiated	ΔE	Unirradiated	Irradiated	ΔE
Nb1-1	202 ± 9	192 ± 4	-10 ± 10	207 ± 3	210 ± 6	3 ± 7
Nb2-1	213 ± 7	197 ± 3	-16 ± 8	217 ± 5	203 ± 7	-14 ± 9
NbZr1-1	202 ± 4	188 ± 3	-14 ± 5	202 ± 5	194 ± 4	-8 ± 6
NbZr2-1	212 ± 3	204 ± 7	-8 ± 8	217 ± 7	213 ± 5	-4 ± 9
Mo1-1	212 ± 5	207 ± 4	-5 ± 6	216 ± 6	214 ± 6	-2 ± 8
Mo1-2	212 ± 5	212 ± 4	0 ± 6	216 ± 6	219 ± 3	3 ± 7
Z1N33A-2	198 ± 3	200 ± 6	2 ± 7	205 ± 3	205 ± 4	0 ± 5
TTZ2M-2	239 ± 3	228 ± 4	-11 ± 5	236 ± 2	225 ± 1	-11 ± 2

The irradiation produced a surface damage layer ~1.65 μm deep. All irradiated samples have higher hardness than unirradiated samples at 1 μm displacement, consistent with irradiation induced hardening. Table 6 summarizes the radiation-hardening at 1 μm indentation depth of the samples. The 2nd batch samples (e.g., Nb2 and NbZr2) exhibited greater hardening than the 1st batch counterparts (Nb1 and NbZr1), which may suggest that the one-step heat treatment of the 2nd batch samples tend to have gerater hardening than the two-step heat treatment of the 1st batch samples. Additionally, the 2nd run irradiation may have resulted in higher radiation hardening as shown by the samples BL-Mo1 irradiated in the 1st and 2nd run. The overall results suggest that TTZ2M, BL-Nb, BL-Mo, BL-NbZr, and Z1N33A have radiation hardening in an ascending order from ~2.5% to ~9.5%, among which the two-step heat treatment is preferred for the BL-series alloys.

Table 6. Nanoindentation-measured radiation-hardening (%) at 1 μm of samples irradiated with Fe^{2+} up to 220 dpa at 475 °C.

Sample	-1 (1st run)	-2 (2nd run)
TTZ2M		2.5
Nb1	3.1	
Nb2	6.5	
NbZr1	4.7	
NbZr2	7.0	
Mo1	4.1	6.7
Z1N33A		9.5

6. CONCLUSIONS AND FUTURE WORK

A total of five ferritic alloys and one ferritic-martensitic steel were designed and fabricated for mechanical property and radiation resistance screening tests. The five ferritic alloys are four 12Cr-3W-3Ni-3Al alloys with varied Zr, Nb and Mo content, with IDs of Z1N33A, BL-Nb, BL-NbZr and BL-Mo, together with a high Zr-content alloy with an alloy ID of Z6. By adjusting the alloy chemistry following the guidance of computational thermodynamics using recently developed database, Laves and B2 phases, together with $Fe_{23}Zr_6$ phase, have been designed to form in the ferritic alloys. Detailed microstructural characterization using optical microscopy, SEM, TEM, and EDS revealed that the phase constituents in the alloys are approximately consistent with their designs. In contrast, the ferritic-martensitic steel with an ID of TTZ2M was designed to have precipitates of $M_{23}C_6$ and MX in the tempered martensite matrix.

Microstructural characterizations of materials after creep and nanoindentation revealed the strengthening and deformation mechanisms of various intermetallic precipitates. In the Z1N33A alloy at elevated temperature, the B2 phase (~30 nm) was found to strengthen the materials through Orowan mechanism, whereas fine precipitates (~250 nm) of the Laves phase can pin dislocations and grain boundaries. The coarse Laves-phase precipitates (in micrometers), however, are detrimental to the creep resistance of the material, with their interface tending to decohesion with the matrix. In the Z6 alloy, both Fe_2Zr phase and $Fe_{23}Zr_6$ phase have higher hardness than the ferritic matrix and forms various types of dislocations in response to deformation. $Fe_{23}Zr_6$ can deform through twinning at room temperature, whereas Fe_2Zr can deform through glide of synchron-Shockley partial dislocations with C36 to C14 phase transformation. Irradiation with 4-MeV Fe^{2+} ions to 50 peak dpa at 400°C resulted in total amorphization of the $Fe_{23}Zr_6$ phase and partial amorphization of the Fe_2Zr, which exhibited indentation responses different from the unirradiated condition.

Microstructure characterizations of the BL-series of alloys showed the effect of alloy elements on precipitates morphology, although the mechanisms remain to be investigated in the near future. It is shown that adding of Mo to the alloy system caused bimodal (~50 nm vs. ~10 nm) distribution of B2 precipitates in size. Alloying with Nb and Zr resulted in Laves-phase precipitates partially coherent to the matrix. The morphology of these precipitates was strongly tailored by the interfacial coherency relationships between the precipitates and the matrix.

Tensile and preliminary creep tests exhibited superior performance of the TTZ2M compared to reference steel T91. The ferritic alloy BL-Nb showed noticeably better creep resistance than TTZ2M in terms of creep rupture life and minimum creep rate. However, mechanical properties of the other ferritic alloys were variable despite their generally similar microstructures compared to the BL-Nb, except for the size difference between the precipitates.

Ion irradiation and post-irradiation examinations shows that the B2 phase in the BL-series of alloys are stable after irradiation whereas the Laves phase underwent amorphization and disintegration as a result of the irradiation at 475°C to a peak damage of 220 dpa. Radiation-induced hardening took place in all the examined alloys with the least hardening in TTZ2M, followed by BL-Nb, and the greatest hardening in Z1N33A. This is in agreement with the increased density of dislocations in irradiated samples as revealed by TEM characterizations. Although the sample surface height measurements indicated varied height changes after the irradiation, multiple factors such as sputtering and surface oxidation would significant influence the results. TEM characterization did not reveal any cavities in the examined alloys, suggesting superior swelling resistance of these alloys compared to T91.

To better understand the microstructure-property relationship, near-term future work will include:

- Characterize the creep-ruptured samples to reveal the effect of particle size (e.g., ~10–50 nm B2; ~250 nm and larger Laves) on their interactions with dislocations and failure;

- Understand the role of Zr and Mo on the formation of the precipitates;
- Optimize and fabricate two larger heats (one TTZ2M and one from the BL-series) for better microstructure control with thermomechanical treatments and detailed assessment.

REFERENCES

[1] S.J. Zinkle, L.L. Snead, Annual Review of Materials Research 44 (2014) 241.
[2] B. Raj, M. Vijayalakshmi, R.J.M. Konings, T.R. Allen, R.E. Stoller, S. Yamanaka, Comprehensive Nuclear Materials, Elsevier, 2012.
[3] L. Tan, Y. Yang, Metallurgical and Materials Transactions A 46 (2015) 1188.
[4] Y. Yang, T. Chen, L. Tan, Computational thermodynamic aided design of novel ferritic alloys, ORNL/TM-2016/229, June 30, 2016.
[5] NRIM Creep Data Sheet, No. 43, National Research Institute for Metals, Japan, 1996.
[6] J. Aufrecht, W. Baumann, A. Leinewever, V. Duppel, E.J. Mittemeijer, Philosophical Magazine 90, (2010) 3149-3175.
[7] L. Tan, Ying Yang, Accelerated development of Zr-containing new generation of ferritic steels for advanced nuclear reactors, ORNL/TM-2015/727, December 2015.
[8] M. Hättestrand, H.-O. Andrén, Acta Mater. 49 (2001) 2123-2128.
[9] L. Tan, J.T. Busby, J. Nucl. Mater. 465 (2015) 724-730.
[10] N. Matsunami, Y. Yamamura, Y. Itikawa, N. Itoh, Y. Kazumata, S. Miyagawa, K. Morita, R. Shimizu, and H. Tawara, in *Energy Dependence of the Yields of Ion-Induced Sputtering of Monatomic Solids*, IPPJ-AM-32 (Institute of Plasma Physics, Nagoya University, Japan, 1983).
[11] J.G. Gigax, T. Chen, H. Kim, J. Wang, L.M. Price, E. Aydogan, S.A. Maloy, D.K. Schreiber, M.B. Toloczko, F.A. Garner, L. Shao, J. Nucl. Mater. 482 (2016) 257-265.
[12] J.E. Jake, C.R. Frihart, J.F. Beecher, R.J. Moon, P.J. Resto, Z.H. Melgarejo, O.M. Suárez, H. Baumgart, A.A. Elmustafa, D.S. Stone, J. Mater. Res. 24 (2009) 1016-1031.